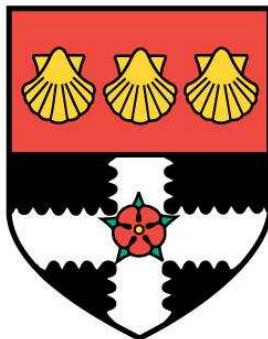# VORTICITY EXTREMES IN NUMERICAL SIMULATIONS OF 2-D GEOSTROPHIC TURBULENCE

ED HAWKINS

Supervisors: Dr. David Stephenson and Dr. Chris Ferro

UNIVERSITY OF READING
Department of Mathematics

August 2005

Disclaimer

I confirm that this is my own work, and the use of all material from other sources has been properly and fully acknowledged.

Acknowledgements

Abstract

A simple numerical model was developed to solve a forced version of the two-dimensional barotropic vorticity equation, on a β-plane stretched around the Earth. The model is designed to produce a turbulent flow and a crude representation of the Northern Hemisphere storm track. The probability distributions of vorticity produced were analysed, with a particular focus on the extreme values attained.

Two different experiments have been performed with the model - firstly without differential rotation ($\beta = 0$), and secondly with a mid-latitude value of β ('geostrophic turbulence'). These experiments produced qualitatively similar turbulence to previous numerical modelling studies - coherent, isolated vortices for $\beta = 0$ and stretched vortices confined to a latitude band for $\beta > 0$, more representative of the real atmosphere.

Through analysis of the statistical moments of the time distributions of vorticity it was shown that higher order moments are dominated by extreme values of vorticity. This has demonstrated that, although commonly used, care should be exercised when using standard moment measures to summarise turbulence. The standard moments were compared with quantile moments and they produced similar results, though the quantile moments are more robust to extreme value outliers. The geostrophic turbulence produces moments that are qualitatively similar to the patterns of observations of White (1980).

Generalised Extreme Value (GEV) probability models were fitted to the extremes of both positive and negative vorticity produced in the model. In the $\beta = 0$ case it was found that the extreme distribution shape parameters of positive and negative vorticity extremes are anti-symmetric, but with a low statistical significance. This effect is also observed in the atmosphere as low pressure systems become more extreme than high pressure systems. However, it was also shown that this effect is initial condition dependent in the model. In the geostrophic case, this asymmetry is not present, though there is a strong latitudinal variation of the extreme distribution shape parameter. Converting the extremes of vorticity to pressure through scaling relations produces values comparable to the extreme pressures observed in the real atmosphere.

Contents

Symbols, Constants and Acronyms

Symbols		units
Relative vorticity	ξ	s^{-1}
Absolute vorticity	ζ	s^{-1}
Coriolis parameter	f	s^{-1}
Latitude	ϕ	rad
Horizontal co-ordinates	(x, y)	
Gradient of Coriolis parameter	$\beta = \partial f / \partial y$	$\mathrm{m}^{-1}\,\mathrm{s}^{-1}$
Reynolds number	Re	
Eddy diffusion parameter	κ	$\mathrm{m}^2\,\mathrm{s}^{-1}$
Horizontal wind vector	$\mathbf{u} = (u, v)$	$\mathrm{m}\,\mathrm{s}^{-1}$
Streamfunction	ψ	$\mathrm{m}^2\,\mathrm{s}^{-1}$
Geopotential height	Φ	km
Forcing	F	s^{-2}
Period of forcing	P	days
Height of forcing 'mountain'	h_0	m
Width of forcing 'mountain'	r	km
Extreme distribution shape parameter	γ	
Extreme distribution location parameter	μ	
Extreme distribution scale parameter	σ	
Typical scaling length scale	L	
Typical scaling horizontal velocity	U	
Atmospheric density	ρ	$\mathrm{kg}\,\mathrm{m}^{-3}$
Atmospheric pressure	p_a	mb

Constants		
Angular rotation rate of the Earth	Ω	7.292×10^{-5} rad s^{-1}
Radius of the Earth	a	6371 km
Acceleration due to gravity	g	9.81 m s^{-2}
Height of flow	H	10 km

Acronyms	
CF	Coriolis Force
GEV	Generalised Extreme Value
IQR	Inter-Quartile Range
PGF	Pressure Gradient Force
PV	Potential Vorticity
RV	Relative Vorticity

Note: In the text, log denotes the natural logarithm.

Chapter 1

Introduction

1.1 Numerical modelling of weather

The science of numerical weather forecasting was started in the early 20th century by Norwegian Vilhelm Bjerknes, and the Bergen Group in Norway. They formulated the basic mathematical equations governing the thermodynamics and hydrodynamics of the atmosphere (Bjerknes 1904), but lacked the technology to solve these equations practically.

The first numerical weather experiment was performed by Richardson (1922), who completed all the calculations by hand. It took over two years to complete - and it was very wrong! Charney et al. (1950) were among the first authors to successfully use a computerised numerical model of the atmosphere. Due to the very limited computing power available they used primitive equations, and just 270 grid points over North America. A 24-hour forecast was produced, with mixed success, but long after the event itself. The results were better than a subjective analysis and demonstrated that this approach was feasible.

Numerical modelling has provided much insight into the physical processes governing the atmosphere by attempting to match the computer simulations with real observed features. As computers became more powerful it was soon possible to incorporate more and more realism into the models and produce real forecasts (i.e. which were actually ahead of the weather). It is now routine for modern supercomputers to perform high-resolution forecasts over the whole globe for days and weeks ahead, and for climate predictions to be made for the coming decades and centuries (e.g. IPCC 2001). The continued, and projected future, increase in computing power will allow finer and finer resolution models to be used, and so probe to smaller scales. It is generally thought that this will increase forecast accuracy (e.g. Lean et al. 2005) as, for example, smaller scale events can be resolved. This might allow better prediction of local extreme weather events, e.g. flooding (Roberts 2005). These events cause the most danger to property and lives, but often occur on a scale smaller than the numerical model resolution, and are often missed, e.g.

the Boscastle floods of 2004.

The motivation for this project was to understand how extremes occur in a simple numerical model. In this context it is ideal to study vorticity, which is a fundamental property of fluid motion.

1.2 Vorticity - definitions and interpretations

1.2.1 Definitions

Vorticity is a measure of local rotation or 'spin density' of a fluid e.g. air, water, and is defined as the circulation per unit area, hence

$$\text{vorticity} = \lim_{A \to 0} \frac{\oint \mathbf{v}.\mathrm{d}\mathbf{l}}{A} = \lim_{A \to 0} \frac{\iint \nabla \times \mathbf{v} \, \mathrm{d}A}{A},$$

by Stokes' theorem, where $\mathbf{v}$ is a velocity, and A is an area. Meteorologists therefore define a quantity called relative vorticity, ξ (Holton 1992), as,

$$\xi = \nabla \times \mathbf{u},$$

where $\mathbf{u}$ is the horizontal wind vector (u, v). This quantity, as its name suggests, is relative to the rotation of the Earth, and this extra rotation adds vorticity. As the velocity of rotation depends on latitude, ϕ, it is natural to define another quantity which includes this extra vorticity. Thus, the absolute vorticity, ζ, is defined as,

$$\zeta = \xi + f,$$

where f is known as the Coriolis parameter,

$$f = 2\Omega \sin \phi,$$

and Ω is the angular rotation rate of the Earth. It is obvious that f is not a constant on a rotating sphere, and describes the differential rotation velocity of the surface of the planet. This differential rotation is often approximated locally by a plane, and this is known as the β-plane approximation, where β is the northward gradient of f,

$$\beta = \frac{\partial f}{\partial y} = \frac{1}{a} \frac{\partial f}{\partial \phi} = \frac{2\Omega \cos \phi}{a},$$

where a is the radius of the Earth. The differential rotation proves crucial to the dynamics of the vorticity in the atmosphere.

1.2.2 Interpretation

In the atmosphere, vorticity is manifested in the pressure systems which dominate the weather in the mid-latitudes. The circulation of the air around these pressure systems is the relative vorticity defined above.
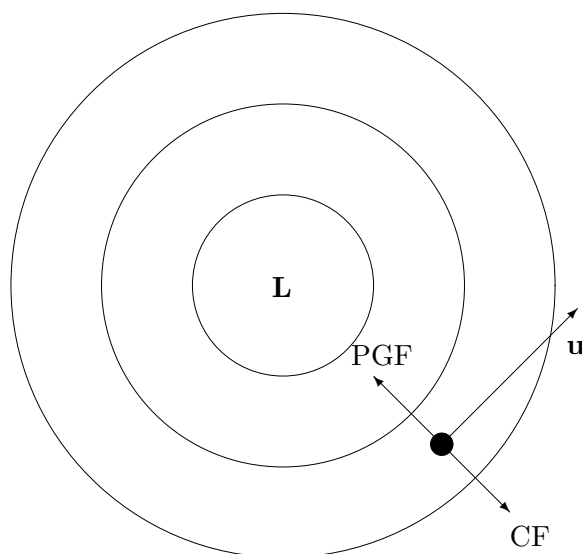
Figure 1.1: Geostrophic balance: The Coriolis Force (CF) balances the Pressure Gradient Force (PGF) causing motion to be anti-clockwise around a low pressure system (**L**) in the northern hemisphere. Circles are isobars (lines of equal pressure) and **u** is the geostrophic wind vector.

In the absence of surface friction effects, the atmosphere is often considered to be in 'geostrophic balance', where the Coriolis Force (CF) balances the Pressure Gradient Force (PGF). The CF is a force due to the Earth's rotation and acts to the right of the velocity of a moving particle in the northern hemisphere, and the PGF is due to the air attempting to return to a equilibrium state of pressure. This causes the air to circulate around a low pressure system in an anti-clockwise direction, and this cyclonic motion is defined as positive vorticity (see Fig. 1.1). Similarly, air will circulate clockwise (anti-cyclonically) around a high pressure system (negative vorticity). The circulating wind is known as the 'geostrophic wind'. The directions of rotation are reversed in the Southern Hemisphere, where the Coriolis Force acts to the left of a moving particle.

1.3 Basics of turbulence

In this study we will use a model which numerically solves the equation which governs the evolution of vorticity in the atmosphere (see Eqn. 3.1), and this equation can describe a 'turbulent' flow. The type of flow of a fluid (see e.g. Batchelor 1967) is characterised by the dimensionless Reynolds number (Re) which is the ratio of the inertial forces to the viscous forces in the fluid. Turbulent flow occurs when Re is large and inertial forces dominate, causing random flow fluctuations which give rise to 'eddies', or vortices. The opposite flow

type is 'laminar flow', which occurs when Re is small and the viscosity dominates - which causes the flow to be constant in time at a particular point. As the atmosphere behaves in a turbulent way, this is what will be simulated.

If $\beta = 0$ and hence f is a constant, then this is described as 'two-dimensional turbulence' (e.g. Kraichnan and Montgomery 1980), and this is used as a first approximation to the atmosphere. If the differential rotation of the planet is introduced (i.e. $\beta > 0$) then this is often described as 'geostrophic turbulence' (e.g. Charney 1971, Rhines 1979), though some authors reserve this term for turbulence in more than one vertical level. Here we solely consider a one-layer model.

It has been shown (e.g. McWilliams 1983, Tung and Orlando 2003) that studying turbulence in two dimensions is a useful analogy for a variety of geophysical phenomena. These phenomena include the large scale structures found in turbulent flow and the limited predictability of the flow, though these authors also note that no universal comparison can be made between the simulations and the real atmosphere.

The vorticity in turbulence, if unforced, will eventually dissipate away and leave a uniform flow field, and many of the idealised numerical studies performed have used unforced equations. The atmosphere generates vorticity through processes such as vortex stretching (Holton 1992), and so this study will add a simulated forcing to keep the numerical model 'alive', and will also produce extreme values of vorticity at times - and in the real atmosphere this would result in severe weather.

Relevant previous studies of turbulence are discussed further in Section 2.3.

1.4 Extreme weather

There is considerable interest in severe (or extreme) weather conditions (e.g. Stott et al. 2004) that are dangerous to property and human life, e.g. heavy rainfall, strong winds, extreme temperatures. It is of course important to be able to predict the location of such events accurately. Current operational forecasting models lack the resolution to resolve small scale extreme weather features, and to improve the predictions would require higher resolution models. Much work is continuing with the aim of increasing the resolution of operational numerical weather forecasting models (e.g. Roberts 2005).

It has long been known (Venn 1887) that certain extreme weather situations are not symmetric - e.g. extreme low pressures are more likely than extreme high pressures. As seen in Fig. 1.1, vorticity and pressure are intimately related, and so this symmetry can be examined in a numerical model of vorticity by testing whether the extremes of positive vorticity are the same as extremes of negative vorticity.

It is also thought that under future climate change extreme weather events are going to become more common (e.g. Easterling et al. 2000, Schär et al. 2004). An increase in the

mean temperature alone will cause an increase in extreme high temperatures, and decreases in extreme low temperatures. It is also believed that there will be a corresponding increase in intense rainfall events (e.g. Easterling et al. 2000). Examining exactly how the extremes change, with time or even latitude, under climate change could be crucial politically, and may aid plans for future mitigation and adaption.

For all these reasons, examining how numerical models cope with extremes is thus a valuable thing to do.

1.5 Project aims

The aim of this project is to use a simple numerical model of vorticity, designed to represent certain aspects of the atmosphere, to examine the extremes of the vorticity generated. More specifically, it will be investigated whether the:

- vorticity behaviour in the model qualitatively matches observations of the atmosphere,
- simulated vorticity extremes depend on latitude and the model parameters,
- extremes are symmetric with respect to the sign of the vorticity.

1.6 Plan of the dissertation

Chapter 2 of this dissertation discusses some of the relevant literature, Chapter 3 describes the features of the numerical model used, and in Chapter 4 the statistical methodology that will be used is defined.

Chapter 5 describes the results using moments of vorticity, and whether the simulation matches the observations. Chapter 6 discusses how the extremes of vorticity depend on latitude, type of turbulence, and whether the extremes are symmetric with respect to the sign of the vorticity. The conclusions and possible future directions are summarised in Chapter 7.

Much of the model design details and model tests are described in Appendix A, and some of the careful statistical tests performed are left to Appendix B.

Chapter 2

Literature Review

2.1 Importance of vorticity

As well as vorticity being a fundamental property of the atmosphere, it is also important as it can be considered a conserved quantity in certain cases. Numerical modelling studies of the atmosphere, like those that are described below, often use conserved quantities to examine the properties of the flow. This is because any changes in the flow are not due to any external change, but are solely due to internal processes moving the quantity. This then provides information on the dynamics and underlying physical principles.

Charney (1971) found a quantity which he called 'pseudo-potential vorticity' (PV) which is conserved with the flow in a model atmosphere. In the model that we will use in this study (see Chapter 3 for the details), the absolute vorticity, ζ, is equivalent to Charney's quantity for a layer of fixed depth (see Section 3.4), and so can be treated as a conserved variable, with the benefits just described.

2.2 Highs and Lows

As already shown (Section 1.2.2) vorticity manifests itself in the atmosphere through the pressure systems that are the dominant cause of the surface weather. Venn (1887) was the first to note that the distribution of pressures in time at a single point is not normally (Gaussian) distributed. He found pressure to be negatively skewed (Fig. 2.1), with low pressure systems observed to depart further from the mean than high pressure systems. He based this result on 4857 successive daily barometer readings in Cambridge, starting on January 1st 1865. Though the main thrust of the letter was to show that any departures from a mean of natural phenomena do not have to be Gaussian, it raised the issue of why low pressures become deeper than high pressures, i.e. low pressures can become more extreme.
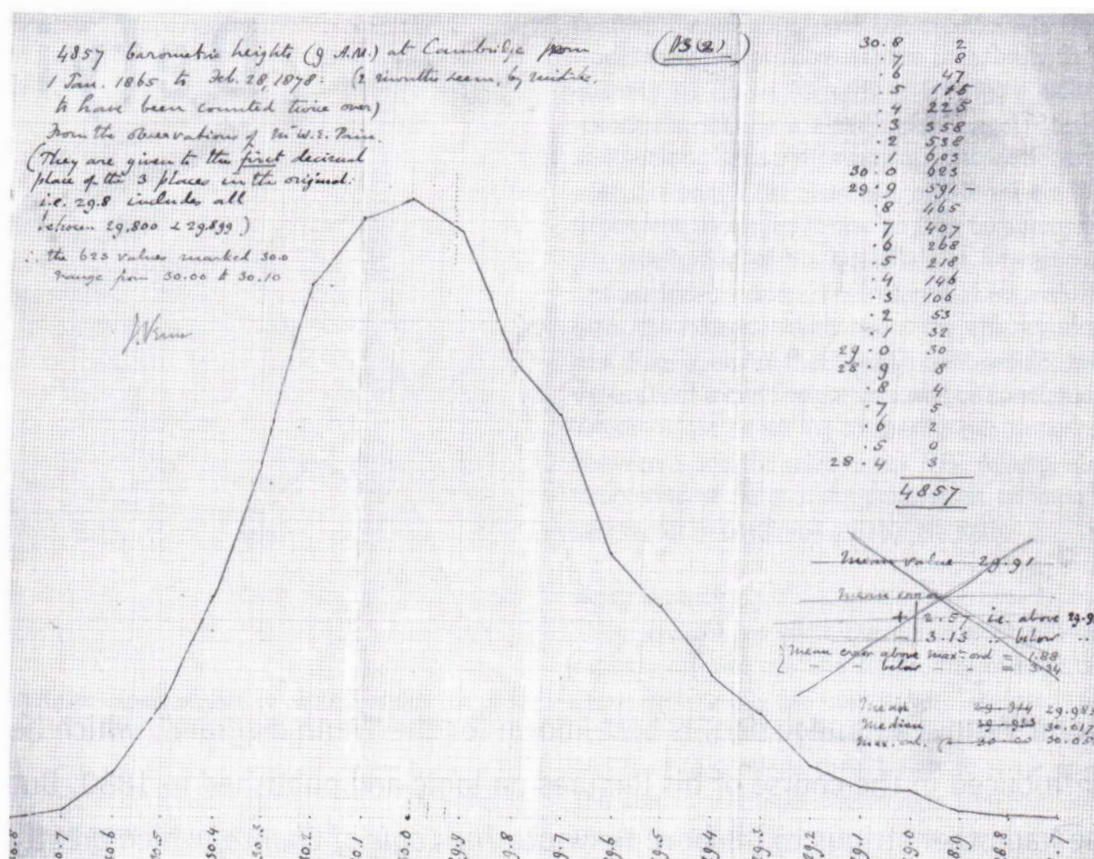
Figure 2.1: Venn's original figure showing the frequency distribution of atmospheric pressures. Pressure increases towards the left. [Reproduced in 'Significance' (June 2005) by permission of the Master and Fellows of Gonville & Caius College, Cambridge.]

Burt (2004) lists the most extreme weather events ever measured, including the record high and low atmospheric pressures. The most extreme high pressure observed was 1086 mb in Mongolia in 2001, and the lowest (non-tornado) pressure was 870 mb in the Western Pacific in 1979. As the mean sea-level pressure is 1013 mb, the record low pressure is twice as far (143 mb) from the mean than the record high (73 mb). Venn (1887) found his similar asymmetry for less extreme pressures. These extremes correspond to values of vorticity of around 10^{-4} (also see Section 6.3).

It is difficult to find detailed explanations for the observation that low pressure systems can become more extreme than high pressure systems. One possible factor is that a force is neglected in the geostrophic balance approximation (Fig. 1.1) - i.e. the centrifugal force. If this force is included then the balance becomes known as 'gradient wind balance'. When attempting to balance these three forces it is shown (e.g. Holton 1992) that larger pressure gradients can be maintained near a low pressure centre than a high pressure centre, thus providing a reason why lows can become deeper.

A possible outcome for this experiment would be to detect a different set of statistical properties in the positive and negative vorticity extremes. As the centrifugal force is neglected in our model approximation we might not expect to see any differences, if the 'gradient wind balance' is the dominant factor in the atmosphere.

2.3   Numerical simulations of turbulence

2.3.1   Two-dimensional turbulence

Rossby (1939) first noted that the atmosphere behaved approximately two-dimensionally when describing what became known as Rossby waves. The main reason why the approximation is a reasonable one is that the atmosphere is a very thin layer (depth $\sim$ 10 km) of fluid on a large planet (radius $\sim$ 6400 km). Also, the vertical motions ($\sim$ cm s^{-1}) in the atmosphere are generally far less than the horizontal motions ($\sim$ m s^{-1}). Finally, rotation of a layer of fluid also tends to lock the fluid into two-dimensional motion, independent of height (the Taylor-Proudman theorem - Proudman 1916) (Kraichnan and Montgomery 1980). Of course it is also far more appealing to study just two dimensions in computer models due to the simplicity and increased speed of calculations.

Fjörtoft (1953) found that in two-dimensional turbulence there has to be a net energy transfer from smaller to larger scales, and this strongly constrains the scale of interactions. The atmosphere clearly acts in a similar way with energy dominating on synoptic (or 'weather system') scales. It was also found that enstrophy (vorticity squared) cascades in the other direction to smaller scales.

Lilly (1969) was the first to numerically simulate two-dimensional turbulence and many authors since have used this paradigm for understanding the atmosphere outside of the tropics.

2.3.2   Geostrophic turbulence

Several authors have noted the importance of the Earth's rotation to the results from two-dimensional turbulence numerical experiments. Rhines (1975) and McWilliams (1984) both showed that the β-effect is vital to limit the scale of vortices in the simulated atmosphere and ocean, and also showed that this limit was a good approximation to the observed size of low and high pressure systems in the mid-latitudes ($\sim$ 1000 km). This is because "... the cascade of pure turbulence to large scales is defeated by wave propagation..." (Rhines 1975). This wave propagation is due to Rossby waves that propagate around the planet as a series of high and low pressure systems. Fig. 2.2 shows a snapshot of 500mb geopotential height field for the Northern Hemisphere and it shows a band of alternating high and low pressure systems around the planet - i.e. Rossby waves.

Wednesday 10 August 2005 00UTC ©ECMWF Forecast t+072 VT: Saturday 13 August 2005 00UTC
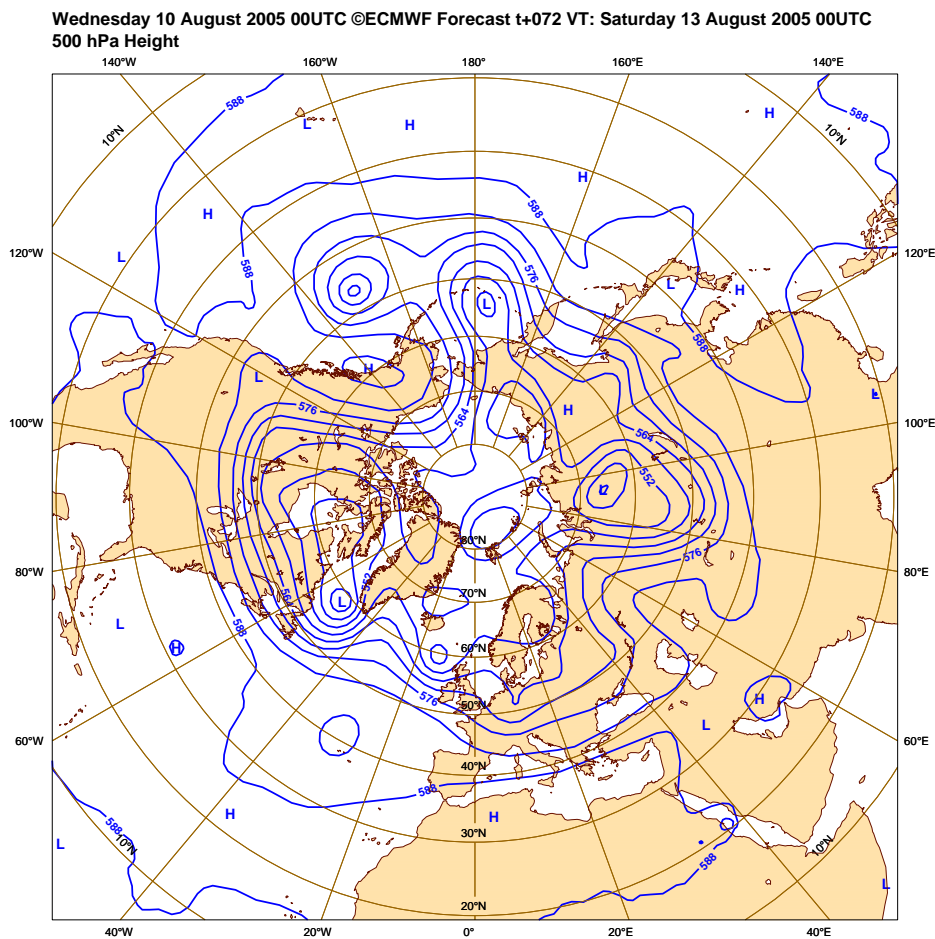**500 hPa Height**

Figure 2.2: Snapshot of the 500mb geopotential height field for the Northern Hemisphere. Source: European Centre for Medium-range Weather Forecasting (ECMWF) website.

Fig. 2.3 shows a snapshot of potential vorticity in the atmosphere which shows the turbulent nature of the atmosphere, with some stretched vortices in the mid-latitudes.

To inject extra realism into the models, many comparisons have been performed (e.g. McWilliams 1990a, McWilliams 1990b) between two-dimensional turbulence and geostrophic turbulence - defined as three-dimensional, rotating, stably stratified flow in this case. This requires a substantial increase in computation time but they find only small differences between the results in the horizontal plane of the two approximations. This is more evidence that the atmosphere behaves in a roughly two-dimensional way.

Tung and Orlando (2003) summarise the issues between using two-dimensional and three-dimensional equations and suggest that there is an over-reliance on two-dimensional models as they lack crucial features like vortex stretching, but acknowledge that many of the features in the atmosphere can be seen in two-dimensional models.
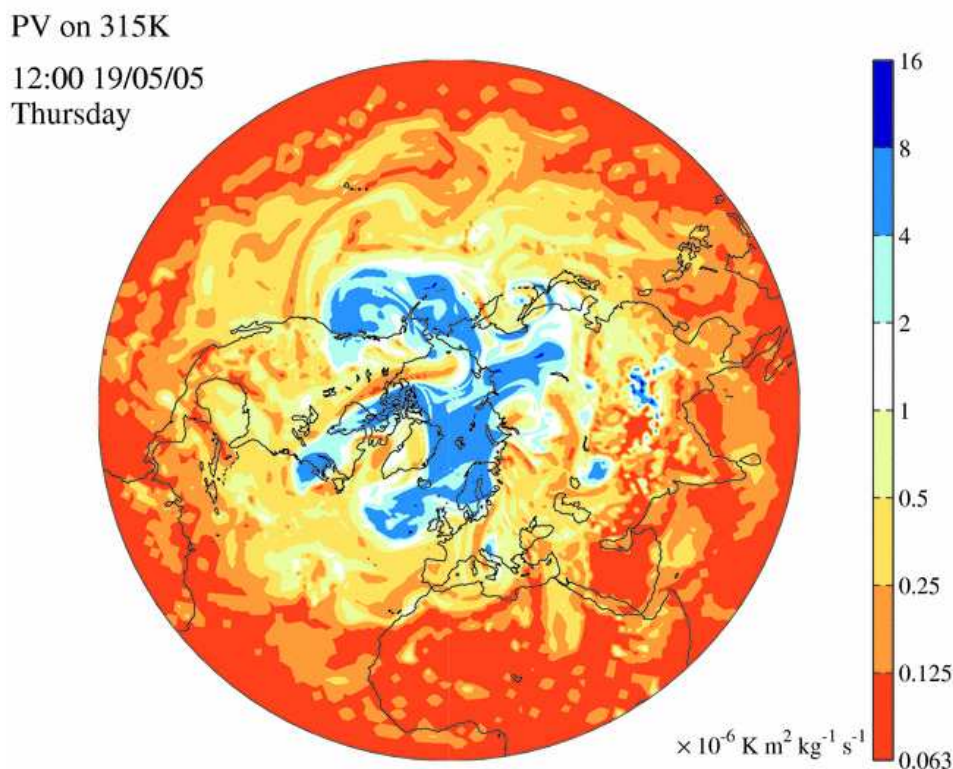
Figure 2.3: Snapshot of Potential Vorticity on the 315 K isentropic (constant temperature) surface for the Northern Hemisphere. Source: Department of Meteorology website.

On a completely different scale, similar equations and numerical modelling techniques have been used to study the turbulence in the giant gaseous planets in the outer solar system - Saturn and Jupiter (e.g. Williams 1978) - especially Jupiter's 'Great Red Spot'.

2.3.3   Statistical results

Previous authors have used the moments described in Section 4.1 to examine the distribution of vorticity in numerical models. McWilliams (1984) used a decaying two-dimensional turbulence model and found that the kurtosis (the fourth moment of a distribution) of ξ averaged in space, increased monotonically with time, but that the distribution of the streamfunction, ψ (see Eqn. 3.2), remained Gaussian. This was found to be due to the formation of coherent isolated vortices which flattened the probability distribution of ξ. When the β-effect was introduced the kurtosis was found to increase in time and then decay back towards a Gaussian value - i.e. it was far less predictable. This was due to β inhibiting the emergence of coherent vortices.

Maltrud and Vallis (1991) experimented numerically with the barotropic vorticity equation on a doubly-periodic domain, which was randomly forced with red noise over a selected wave-number range. They also found that the β-effect limited the formation of coherent

vortices. They found significantly increased values of kurtosis whenever coherent vortices are formed when averaging over the spatial domain. As β is increased the kurtosis decreases towards that of a normal (Gaussian) distribution, as the flow becomes more anisotropic and there are fewer coherent vortices.

Much of the turbulence literature concentrates on the evolution of the energy spectrum to see if the theoretical and observational constraints can be modelled, rather than the distribution of vorticity itself. This is also usually done in weakly decaying turbulence with no forcing. This experiment is therefore fairly unique and, as will be seen, can reproduce certain features of the atmosphere well.

2.4 Atmospheric observations

It is of course important to verify in at least a qualitative way that the atmosphere does behave in a similar way to the numerical simulations. In the mid-latitudes there exists a 'storm track' - an elongated region where pressure systems are more likely to form. This is especially true in winter, generally across the Atlantic and Pacific oceans, and positioned roughly at a latitude of 45°N. Fig. 2.4 shows a proxy for the storm track strength. The shaded areas indicate the regions where storms are more intense, and shows the two clear tracks across the Northern Hemisphere oceans. These pressure systems bring a lot of varying weather to the UK and so analysing them has been of some considerable interest (e.g. FASTEX).
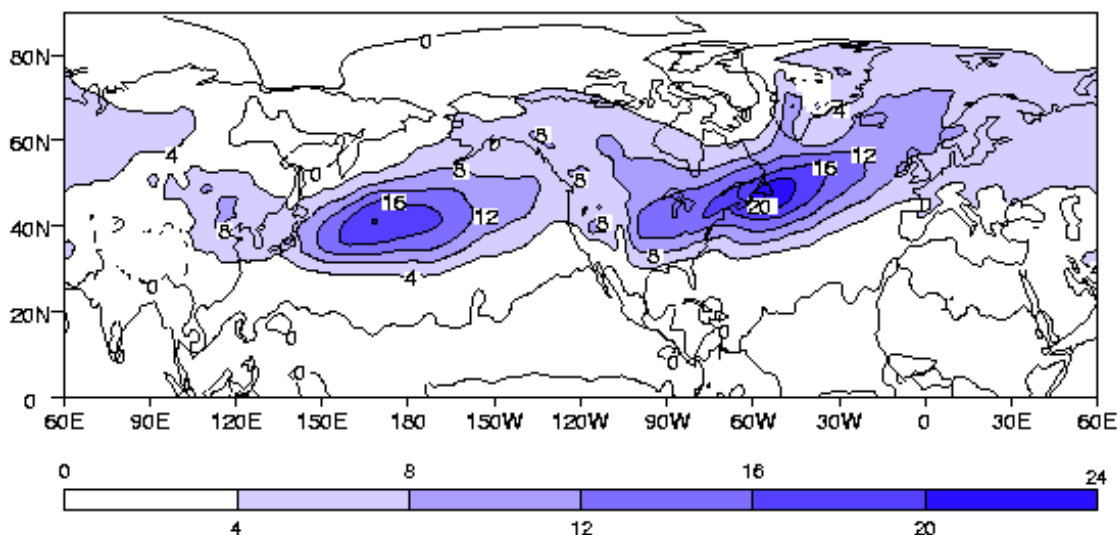

Figure 2.4: Storm track strength - the poleward transient temperature flux on the 700mb surface - from European Centre for Medium-range Weather Forecasting (ECMWF) data. Credit: Len Shaffrey, University of Reading.

2.4.1 Skewness

White (1980) used twelve years (1965 – 1976) of data from the National Meteorological Center analyses to calculate the statistics of the distribution of geopotential height - the altitude of a particular isobar - over the Northern Hemisphere. He found that in many regions these distributions in time were non-normal. He found skewness (the third moment of a distribution - see Section 4.1) was positive at high latitudes and negative at low latitudes (Fig 2.5).

More recently, Swanson (2001) analysed forty years (1958 – 1998) of winter (January and February) potential vorticity fields on isentropic (constant temperature) surfaces in the Northern Hemisphere. This data was taken from the National Centers for Environmental Prediction re-analysis fields. He found that there are were large differences between the time mean and time mode of vorticity. It was also found that there are large latitudinal variations in the distribution of potential vorticity, and these distributions become more skewed and bimodal as the latitude increases.

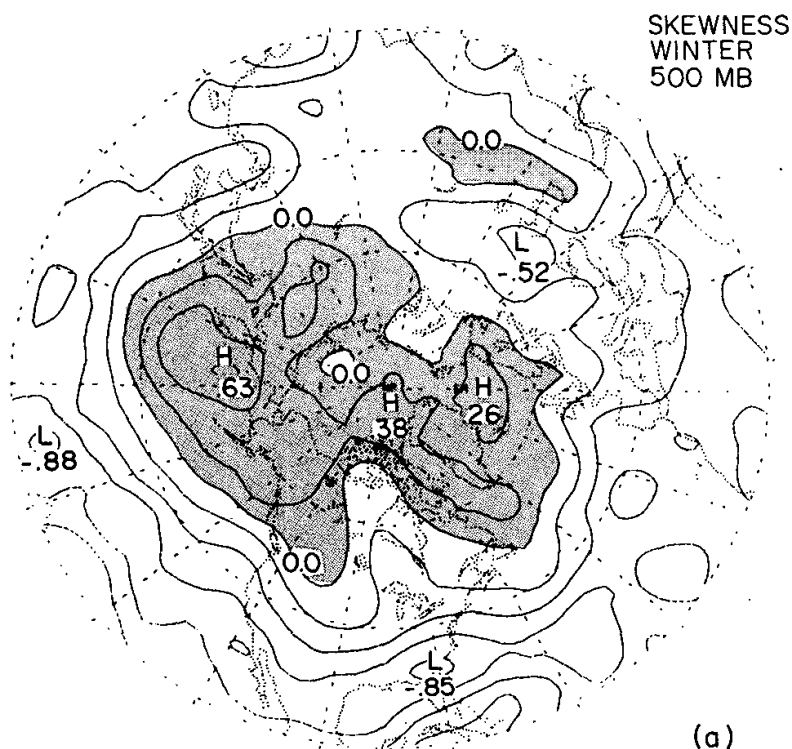Nakamura and Wallace (1991) found that the skewness of geopotential height was pos-

Figure 2.5: Fig. 1a from White (1980) showing winter (November – February) skewness over the Northern Hemisphere. Shaded areas are positive skewness, and these areas are found at higher latitudes.

itively skewed north of the storm track, and negatively skewed southwards. They also noted that "extreme events" (which they defined as outside 3 standard deviations of the mean) accounted for about half of the negative skewness at lower latitudes, whereas "large events" (defined as between $2 - 3$ standard deviations from the mean) are responsible for the other half of the skewness at low latitudes, and nearly all the skewness at high latitudes.

All of White (1980), Swanson (2001) and Nakamura and Wallace (1991) therefore observed an increase in skewness with latitude of the atmospheric quantity under test. The crossover between positive and negative skewness occurred between 30 - 45°N.

2.4.2 Kurtosis

White (1980) found that the kurtosis (the fourth moment of a distribution - see Section 4.1) of geopotential height was larger than for a normal (Gaussian) distribution in the high and low latitudes (Fig. 2.6), and smaller than for a normal distribution in the mid-latitudes. The maps are rather noisy and the low latitudes have the highest levels of significance. He also noted that high kurtosis tends to be seen with significantly non-zero values of skewness.
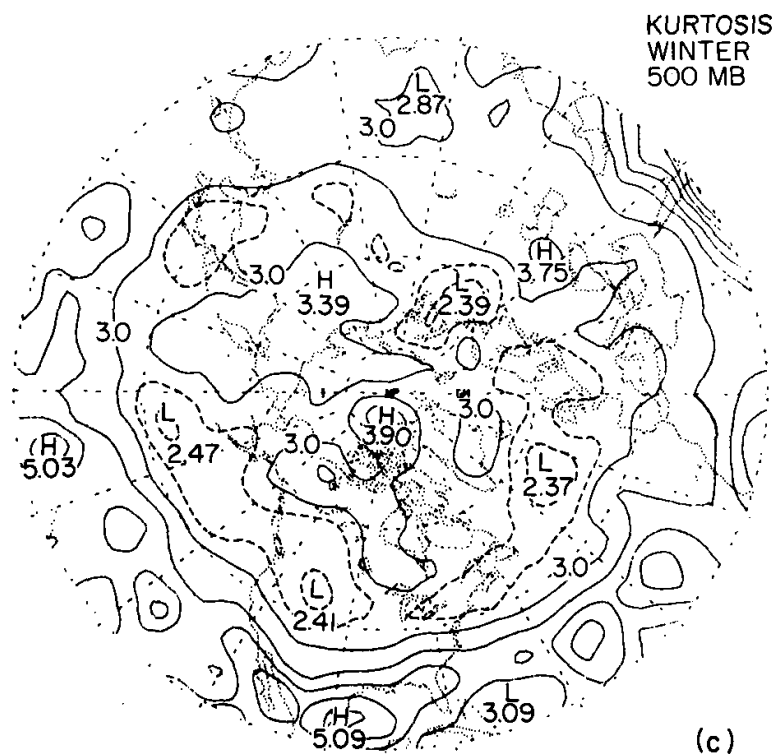

Figure 2.6: Fig. 1c from White (1980) showing winter (November – February) kurtosis over the Northern Hemisphere. Solid contours are for kurtosis values larger than 3. Dashed lines are for kurtosis values smaller than 3.

2.5   Summary

In this Chapter some of the literature relevant to this study has been considered. It has been shown that the atmosphere acts like a turbulent flow, and it has been discussed how numerical models of two-dimensional and geostrophic turbulence have been used to simulate features of the atmospheric system. The statistical results of these simulations, such as the large values of kurtosis found in turbulence models, will be compared with the results of this project.

Some observations of the statistics of vorticity in the atmosphere have been summarised - these include the observation that the distribution of atmospheric pressures is not symmetric, and that the skewness of the distribution of vorticity increases with latitude. These observations will be compared to the time evolution of the vorticity in the numerical model developed in this study.

Chapter 3

Numerical Model Development

This Chapter describes the numerical model that is used in this study. It is a much modified version of the model written for the Department of Meteorology 'Numerical Modelling' module, MTMW14.

3.1 Designing the numerical model

There are many factors which influence the design of the model to be used. The model chosen is a two-dimensional solution (for the reasons given in Section 2.3.1) to the barotropic vorticity equation (see Eqn. 3.1 below). The reason for this choice is that this is the simplest possible model to simulate a mid-latitude storm track.

The model is not designed to produce forecasts, but just to analyse the statistics of the distribution of vorticity. For this reason all surface friction effects are ignored, so we assume that the model is in geostrophic balance. The equations are solved on a β-plane, which assumes that the Coriolis parameter, f, varies linearly with latitude in the region under test. For small ranges of latitude this is a reasonable, and commonly used approximation.

3.1.1 Barotropic vorticity equation

The governing equation for the evolution of vorticity can be derived from the momentum equations on a rotating sphere. The atmosphere is a very thin fluid in comparison to the size of the planet and can, to a first approximation be considered as two-dimensional. Another common approximation that can be made is to assume that the atmosphere is barotropic, i.e. the density depends solely on the pressure. Assuming an incompressible fluid in geostrophic balance and under barotropic conditions the vorticity is governed by the barotropic vorticity equation (see e.g. Kraichnan and Montgomery 1980, Holton 1992), which is

$$\frac{\partial \xi}{\partial t} + \mathbf{u}.\nabla \xi + \beta v = 0.$$

In reality, the atmosphere generates and dissipates vorticity due to processes such as radiation, convection and mixing. Adopting a very simplistic model for diffusion and forcing changes the right hand side of the barotropic vorticity equation, which then becomes

$$\frac{\partial \xi}{\partial t} + \mathbf{u}.\nabla \xi + \beta v = \kappa \nabla^2 \xi + F, \tag{3.1}$$

where κ is the eddy diffusion parameter, and F is a forcing term to be discussed in Section 3.2.

McWilliams (1984) experimented with a different model of diffusion - hyperdiffusion ($\nabla^4 \xi$ instead of $\nabla^2 \xi$, on the right hand side of the barotropic vorticity equation - Eqn. 3.1) and found that it made little difference to the evolution of the vorticity in his numerical experiments.

3.1.2 Physical relationships of variables

To build our model of the atmosphere we consider the physical equations required. To generate a zonal flow in the model atmosphere, the initial $500\,\mathrm{mb}$ geopotential height (the altitude of the $500\,\mathrm{mb}$ isobar) field, Φ, has a constant gradient with latitude. This geopotential height can be converted into a streamfunction, ψ, using the relation,

$$\psi = \frac{g}{f_0}\Phi, \tag{3.2}$$

where g is the acceleration due to gravity, and f_0 is the Coriolis parameter for the chosen central latitude. The streamfunction then also has a gradient with latitude, and can be used to calculate the wind velocities (assuming geostrophic balance) via the equations,

$$u = -\frac{\partial \psi}{\partial y}, \qquad v = \frac{\partial \psi}{\partial x}, \tag{3.3}$$

and to calculate the relative vorticity, ξ, using the Poisson equation,

$$\xi = \nabla^2 \psi, \tag{3.4}$$

which can then be used in the barotropic vorticity equation (Eqn. 3.1).

3.2 Forcing

Without some addition of vorticity into the model the diffusion term will cause the vorticity to decay and disappear. In the atmosphere, vortex tube stretching and compressing can generate vorticity (Holton 1992) when a flow passes over some orography (hills and mountains). To inject vorticity into the model we therefore use a sinusoidally varying forcing based on these orographic effects. The forcing (F) term in the barotropic vorticity equation (Eqn. 3.1) is then,

$$F = -\frac{f_0}{H}\sin\left(\frac{2\pi t}{P}\right)\mathbf{u}.\nabla h, \tag{3.5}$$

where t is the elapsed time, P is the forcing period, H is the uniform depth of the flow,

$$h(x, y) = h_0 \exp\left(-\frac{d^2}{2r^2}\right), \qquad (3.6)$$

and

$$d^2 = (x - x_0)^2 + (y - y_0)^2,$$

which describes an oscillating, circular Gaussian 'hill' with height, h_0 and characteristic width, r, centred at (x_0, y_0). The derivatives of h can be calculated analytically from Eqn. 3.6.

The symmetric nature of the forcing means that equal amounts of positive and negative vorticity are injected into the model. The forcing is present in one location in the channel, and we examine the vorticity effects produced downstream from the forcing away from its direct effects. The height and width of the 'hill' is chosen to be realistic for a range of mountains. A typical value for the height was $h_0 = 2500\,\mathrm{m}$, the width, $r = 800\,\mathrm{km}$, and the depth of the flow was assumed to be $H = 10\,\mathrm{km}$, which is the approximate depth of the troposphere. A typical length for the forcing period, P, was 3 days. The choice of these parameters is described further in Appendix A.2.

The forcing is placed at the left end of the channel with its centre at $(x_0 = 50, y_0 = 64)$. Thus the right end of the channel should be clear of any direct forcing effects, and any features should be solely due to the nature of the turbulence created.

3.3   Numerical model construction

The general principle of the model developed was to evolve the relative vorticity in time, and at each time-step solve the Poisson equation (Eqn. 3.4) to calculate the new stream-function and wind velocities which are required in the next step of the numerical scheme. The steps are described in more detail in Appendix A.1.1.

Much testing was performed using different grid sizes to find an optimal choice for this study. It was found that the channel had to be wider than expected to ensure that the central regions were not affected by boundary effects. The model grid chosen consists of 256×128 points in the longitude (x) and latitude (y) directions respectively, and this is limited by time and disk space constraints.

The horizontal resolution is chosen to be $\Delta x = \Delta y = 110.6\,\mathrm{km}$ between grid points in each direction - this stretches the β-plane around the planet at a latitude of 45°N (see Fig. 3.1). This results in a channel of approximately 120° of latitude width.
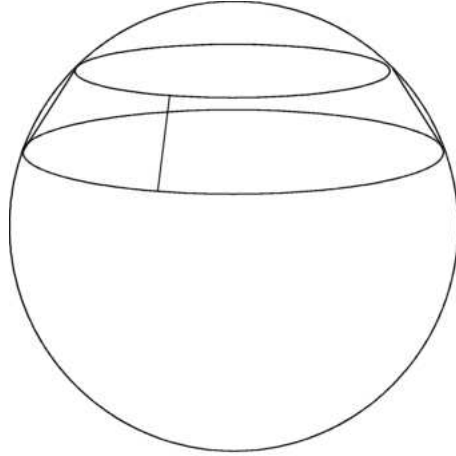
Figure 3.1: Diagram showing the geometrical set up of the model with a latitude band wrapping around the globe.

3.3.1 Choosing the numerical scheme

The barotropic vorticity equation (Eqn. 3.1) includes both an advection term and a diffusion term. It is known that a centred time, centred space (CTCS) scheme is unstable with respect to a diffusion term, and that a forward time, centred space (FTCS) scheme is unstable with respect to an advection term. We therefore need to look for an alternative. Choosing the CTCS scheme, but putting the diffusion term on a different time level is an obvious choice. But which level? One of the main constraints for this project is simplicity and efficiency, and so we require an explicit scheme, which requires choosing the $n-1$ level for the diffusion term.

The finite difference scheme chosen to approximate Eqn. 3.1 is therefore,

$$
\begin{aligned}
\frac{(\xi_{l,m}^{n+1} - \xi_{l,m}^{n-1})}{2\Delta t} &+ \frac{u_{l,m}^n}{2\Delta x}(\xi_{l+1,m}^n - \xi_{l-1,m}^n) + \frac{v_{l,m}^n}{2\Delta y}(\xi_{l,m+1}^n - \xi_{l,m-1}^n) + \beta v_{l,m}^n \\
&= \kappa \left(\frac{\xi_{l+1,m}^{n-1} - 2\xi_{l,m}^{n-1} + \xi_{l-1,m}^{n-1}}{(\Delta x)^2} + \frac{\xi_{l,m+1}^{n-1} - 2\xi_{l,m}^{n-1} + \xi_{l,m-1}^{n-1}}{(\Delta y)^2} \right) \\
&- \frac{f_0}{H} \sin\left(\frac{2\pi t}{P}\right) \left(u_{l,m}^n \frac{\partial h}{\partial x} + v_{l,m}^n \frac{\partial h}{\partial y} \right),
\end{aligned} \tag{3.7}
$$

where n is the time level, l is the x-level and m is the y-level. This is a mixed level scheme and can be re-arranged to give $\xi_{l,m}^{n+1}$ in terms of known quantities at time levels n and $n-1$. The first time step is done as a forward scheme in time, replacing all the $n-1$ with n in the above equation. The design and testing of the algorithm to perform this scheme is described in Appendix A.1, and the choice of time-step is described in Appendix A.2.1.

3.3.2 Initial conditions

The background initial geopotential height field, Φ, is a linearly varying field with a gradient chosen to produce roughly the correct magnitude of easterly zonal flow ($u \sim 30\,\mathrm{m\,s}^{-1}$) in the channel. The model is started with a Gaussian distribution of random noise of relative vorticity imposed on the zonal flow. The width of the random distribution is chosen to mimic the distribution of vorticity in the atmosphere - a typical value for the width used was 10^{-4}.

3.3.3 Boundary conditions

The experimental setup requires that the boundary conditions in the x-direction (E-W) to be periodic so that the channel is continuous. In the y-direction (N-S) we assume 'free-slip' boundary conditions so that there is no flow across the frictionless boundaries,

$$v = 0, \tag{3.8}$$

$$\frac{\partial u}{\partial y} = 0. \tag{3.9}$$

The size of the domain under test is chosen so that the channel is wide enough to ensure that the boundary effects are negligible in the centre of the channel. The change of horizontal scale with latitude is ignored so that the equations can be solved on a standard Cartesian grid.

3.4 Potential vorticity

As discussed in Section 2.1 it would be useful to examine a conserved physical quantity in the model. Here we show that the absolute vorticity, ζ can be considered as potential vorticity, and thus conserved.

The absolute vorticity on a β-plane is defined by,

$$\zeta = \xi + f = \xi + \beta y, \tag{3.10}$$

and the Lagrangian time derivative of ζ, in two dimensions, is

$$\frac{D\zeta}{Dt} = \frac{\partial \zeta}{\partial t} + u\frac{\partial \zeta}{\partial x} + v\frac{\partial \zeta}{\partial y}. \tag{3.11}$$

By substituting Eqn. 3.10 into Eqn. 3.11 and using the relations,

$$\frac{\partial f}{\partial y} = \beta,$$

$$\frac{\partial f}{\partial x} = 0,$$

we find that,

$$\frac{D\zeta}{Dt} = \frac{\partial \xi}{\partial t} + u\frac{\partial \xi}{\partial x} + v\frac{\partial \xi}{\partial y} + \beta v.$$

From Eqn. 3.1 this can be rewritten as,

$$\frac{D\zeta}{Dt} = \kappa \nabla^2 \xi + F,$$

and in the limit of small diffusion and away from the forcing region,

$$\frac{D\zeta}{Dt} \approx 0,$$

and thus the absolute vorticity, ζ, can be considered as a conserved Lagrangian quantity. It is also the potential vorticity (PV) for this constant thickness single layer atmosphere.

3.5 Summary

This Chapter has described the numerical model that will be used in this study. The two-dimensional barotropic vorticity equation is solved on a 256×128 grid, for two situations - $\beta = 0$ and $\beta > 0$. Much testing was performed to choose an optimal parameter set which would give valuable results, but would not be too expensive in CPU time and disk space. More details of this testing is given in the Appendices.

Chapter 4

Statistical Methodology

This Chapter defines and describes the statistical methodology that is going to be used to investigate vorticity in the model simulations.

4.1   Moments

The sample moments, m_k, of a random variable ξ are defined as,

$$\overline{\xi} = \frac{1}{n} \sum_{i=1}^{n} \xi_i,$$

$$m_k(\xi) = \frac{1}{n} \sum_{i=1}^{n} (\xi_i - \overline{\xi})^k \qquad \text{for } k \geq 2,$$

where the mean is denoted by $\overline{\xi}$. The standard deviation, skewness and kurtosis are defined respectively as,

$$s = \sqrt{m_2},$$
$$b_1 = \frac{m_3}{s^3},$$
$$b_2 = \frac{m_4}{s^4}.$$

The standard deviation measures the width of a distribution, the skewness measures the degree of asymmetry and the kurtosis is a measure of the flatness of the distribution. A normal (or Gaussian) distribution has skewness $b_1 = 0$ and kurtosis $b_2 = 3$. A distribution with a higher peak ($b_2 > 3$) is known as leptokurtic, and a flat distribution ($b_2 < 3$) is known as platykurtic.

These are standard statistics and have been calculated for various observations of the atmosphere, such as vorticity (Swanson 2001) and geopotential height (White 1980). Estimating these for the model will allow a comparison between the model and the observations. They are also easy to calculate, and this can be done throughout the model run from the cumulative sums without knowing the mean beforehand (Smith 1995).

4.2 Quantile moments

The standard moments just described can be particularly sensitive to extreme values of the variable under test. Quantile moments are defined differently to be more resistant to these outliers, especially for the higher order moments (Moors 1988).

The i-th quartiles (Q_i) and j-th octiles (E_j) of a distribution of a random variable X, are defined as the largest quantities which fufil the criteria,

$$Pr(X < Q_i) \leq i/4 \qquad \text{for } i = 1, 2, 3$$
$$Pr(X < E_j) \leq j/8 \qquad \text{for } j = 1, \dots, 7$$

where Pr is probability. This leads to the definitions (Moors 1988) of the quantile moments,

$$\text{median} = Q_2,$$
$$\text{half inter quartile range} = (Q_3 - Q_1)/2,$$
$$\text{quartile skewness} = \frac{(Q_3 - 2Q_2 + Q_1)}{Q_3 - Q_1},$$
$$\text{quartile kurtosis} = \frac{(E_7 - E_5) + (E_3 - E_1)}{E_6 - E_2}.$$

Note that a Gaussian distribution has a quantile kurtosis of about 1.235.

These moments are not so easy to calculate in the model as the data at every timestep needs to be stored, which is prohibitive on disk space. They will be used on a fraction of the grid to allow a comparison with the standard moments.

4.3 Extreme value modelling

A key part of this research is to examine the extremes of vorticity that the numerical model produces to allow comparisons with observations and to determine the dependence of extremes on parameters such as β, and latitude. For this it is necessary to examine the tails of the distribution in detail, rather than the results being affected by the rest of the distribution. This type of analysis has been used in meteorology to determine the chances of extreme events, e.g. rainfall (Nadarajah 2005), wind (Palutikof et al. 1999) - though it has not been performed on the observations of vorticity in the atmosphere, or in previous numerical models of atmospheric turbulence.

4.3.1 Definitions

The generalised extreme value (GEV) distribution is used as a good approximation to the frequency distribution of a sample of maxima (e.g. Coles 2001) - assuming the maxima

are taken over a sufficiently large time interval. Similar theoretical arguments apply to the distribution of minima and so comparisons can be made between extreme positive and extreme negative vorticity. This is especially interesting considering the observed asymmetry in the distribution of sea level pressures in the atmosphere (Section 2.2).

The GEV distribution function (e.g. Coles 2001), $G(z)$, is

$$G(z) = \exp\left[-\left\{1 + \gamma\left(\frac{z-\mu}{\sigma}\right)\right\}^{-1/\gamma}\right], \tag{4.1}$$

where γ is the shape parameter, μ is the location parameter, and σ is the scale parameter. The parameters satisfy the conditions

$$-\infty < \gamma, \mu < \infty,$$
$$\sigma > 0,$$
$$\left(1 + \gamma\frac{(z-\mu)}{\sigma}\right) > 0.$$

This GEV, with its three parameters, is used as a summary of the distribution of extreme vorticities. Fig. 4.1 shows three examples of the GEV distribution for $\mu = \sigma = 1.0$ and a varying shape parameter, γ.
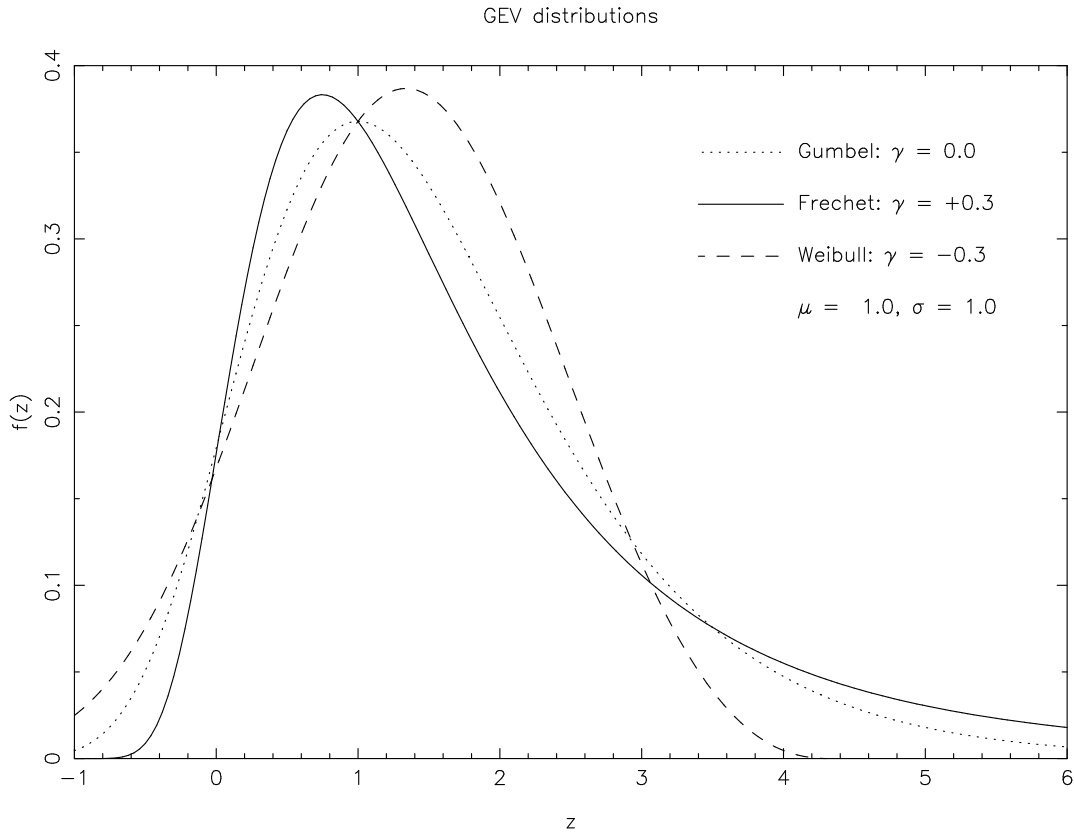

Figure 4.1: Plot of density functions for different classes of the GEV distribution as labelled. Each curve has the same location (μ) and scale (σ) parameters.

There are three classes of the extreme value distribution. Jenkinson (1955) first showed that these three classes could be written in one parametric form - the GEV distribution. The class to which the data belongs depends on the value of the estimated shape parameter γ, and they are defined and named as,

$$\text{Fréchet}: \ \gamma > 0,$$
$$\text{Weibull}: \ \gamma < 0,$$
$$\text{Gumbel}: \ \gamma = 0,$$

and these classes each have different distribution tail characteristics. For the Weibull class the upper end point of the distribution is finite,

$$z_+ = \mu - \frac{\sigma}{\gamma}, \tag{4.2}$$

whereas the Gumbel and Fréchet classes have an infinite upper bound. The sharp upper limit cutoff for the Weibull distribution is easily seen in Fig. 4.1.

4.3.2 Finding an optimal block size

The GEV distributions theoretically describe the shape of the distribution of maxima (or minima), rather than all the data. It is therefore necessary to split the time series data into blocks (e.g. daily, monthly, annually) and find the maxima in each block to use as the independent, sorted variables, z. The GEV distribution is then fitted to these maxima.

The block size chosen will affect the results so it is also necessary to find an optimal size. If the blocks are too small then the GEV may be a poor representation of the data, and there will be a bias in the results. If the blocks are larger then the errors on the parameter estimates will increase as there are fewer points to fit the distributions to. Some experimentation is required to find the optimal block size, and this size will depend on the data being used. Essentially this involves trying a wide range of block sizes and checking how the shape parameter depends on block size.

It can be shown that if the GEV is a good representation of the data then the shape parameter will remain constant with block size. From Eqn. 4.1,

$$Pr(M_n < z) = \exp[-\{1 + \gamma_n(z - \mu_n)/\sigma_n\}^{-1/\gamma_n}],$$

where M_n is the maximum of independent variables $Z_1, Z_2, ..., Z_n$, then

$$Pr(M_{kn} < z) = Pr(M_n < z)^k,$$

which can be rearranged to give,

$$\gamma_{kn} = \gamma_n,$$
$$\sigma_{kn} = \sigma_n k^{\gamma_n},$$
$$\mu_{kn} - \sigma_{kn}/\gamma_{kn} = \mu_n - \sigma_n/\gamma_n,$$

and so γ remains constant with block size. A suitable block size can hence be chosen by finding the smallest block size where the shape parameter becomes constant with increasing block size. The choice for our model is described in Appendix B.3.

4.3.3 Estimating the GEV parameters

Assuming that there are m independent maxima, z_i for $1 \leq i \leq m$, then the log-likelihood estimate for the GEV parameters, when $\gamma \neq 0$ is (Coles 2001)

$$\ell(\hat{\mu}, \hat{\sigma}, \hat{\gamma}) = -m \log \hat{\sigma} - \left(1 + \frac{1}{\hat{\gamma}}\right) \sum_{i=1}^{m} \log \left[1 + \hat{\gamma} \left(\frac{z_i - \hat{\mu}}{\hat{\sigma}}\right)\right]$$
$$- \sum_{i=1}^{m} \left[1 + \hat{\gamma} \left(\frac{z_i - \hat{\mu}}{\hat{\sigma}}\right)\right]^{-1/\hat{\gamma}}, \tag{4.3}$$

and maximising this equation with respect to the parameter estimates $(\hat{\mu}, \hat{\sigma}, \hat{\gamma})$ gives the maximum likelihood estimate for the entire GEV family of distributions. Care is required when maximising the above equation as many parameter combinations cause the second term to be imaginary. A standard minimisation routine in MATLAB allowed the parameters to be estimated.

An alternative method of estimation is due to Hosking et al. (1985, hereafter HWW85) and uses an approximate closed form estimate for the GEV parameters,

$$-\hat{\gamma} = 7.8590c + 2.9554c^2,$$
$$\hat{\sigma} = \frac{-(2d_1 - d_0)\hat{\gamma}}{\Gamma(1 - \hat{\gamma})(1 - 2^{\hat{\gamma}})}, \tag{4.4}$$
$$\hat{\mu} = d_0 - \frac{\hat{\sigma}(\Gamma(1 - \hat{\gamma}) - 1)}{\hat{\gamma}},$$

where Γ is the Gamma function and

$$c = \frac{2d_1 - d_0}{3d_2 - d_0} - \frac{\log 2}{\log 3},$$
$$d_r = \frac{1}{m} \sum_{j=1}^{m} \frac{(j-1)(j-2)\cdots(j-r)}{(m-1)(m-2)\cdots(m-r)} z_j.$$

The approximate variance of the parameters using the closed form solution (HWW85) are,

$$\text{var}(\hat{\gamma}) = w_{33}/m$$
$$\text{var}(\hat{\sigma}) = \hat{\sigma}^2 w_{22}/m$$
$$\text{var}(\hat{\mu}) = \hat{\sigma}^2 w_{11}/m$$

where the w_{ii} are dependent on the value of $\hat{\gamma}$, and the values of w_{ii} are given in Table 1 of HWW85, and are interpolated between the values given. The square root of the variances will give the usually quoted standard errors.

This closed form approximation is easier and faster to implement than the maximum likelihood method, and also allows easy estimates of the error on the calculated parameters, but it is an approximation. Both the maximum likelihood and closed form estimates will be used initially to check the results are consistent between methods but the closed form will be used predominantly as it will be seen to give essentially the same results as the maximum likelihood method.

4.3.4 Verification

It is also necessary to ensure that the best fit GEV distribution is actually a good fit to the data. This is achieved by the use of probability plots, quantile plots and return level plots.

Probability plots

This is a comparison of the empirical and fitted distribution functions. The empirical distribution function is given by,

$$\tilde{G}(z_i) = \frac{i}{m+1} \quad \text{for } i = 1, \ldots, m,$$

as this gives the probability of an observation being less than z_i. The fitted model distribution function is given by Eqn. 4.1, using the fitted model parameters, and this is denoted by $\hat{G}(z_i)$. The probability plot is then $(\tilde{G}(z_i), \hat{G}(z_i))$. If this is close to a straight line then the fit is a good one, and any deviations might provide insight into a process or series of events which cause the deviation.

Quantile plots

Probability plots space the data linearly, whereas it can sometimes be more useful to carefully examine the extremes of the block maxima. To highlight a different part of the distribution quantile plots are used. Defining,

$$\hat{G}^{-1}\left(\frac{i}{m+1}\right) = \hat{\mu} - \frac{\hat{\sigma}}{\hat{\gamma}}\left(1 - \left[-\log\left(\frac{i}{m+1}\right)\right]^{-\hat{\gamma}}\right),$$

the quantile plot is then,

$$\left(\hat{G}^{-1}\left(\frac{i}{m+1}\right), z_i\right) \quad \text{for } i = 1, \ldots, m.$$

Again, a straight line indicates a good fit.

Return level plots

Perhaps the simplest to understand, the return level plots give an indication of how often an event might recur in terms of its return period. These are often quoted as, for example, a 'once in 10-year event'. The data is plotted as $([m+1]/i, z_i)$ and the model is plotted as $(1/p, z_p)$ where $\hat{G}(z_p) = 1 - p$, and

$$z_p = \hat{\mu} - \frac{\hat{\sigma}}{\hat{\gamma}} \left(1 - [-\log(1-p)]^{-\hat{\gamma}} \right).$$

Thus p is the probability that a maximum exceeds z_p, and so has the range, $0 < p < 1$.

The data should lie close to the model line, and extrapolating the model can give estimates of the chances of very extreme events, though these must be treated with caution, especially if the time series used to generate the maxima has an insufficient span.

4.3.5 Extreme minima

The methods outlined above can also be used to examine extreme minima as well as extreme maxima. This is achieved by using the negative of the block minima as z_i, and repeating the analysis. Comparing the behaviour of the minima and maxima might provide insights into the processes which cause the differences (if any) between them.

4.4 Summary

In this Chapter the standard moments that have been used by previous authors in observational and numerical simulation studies have been defined. They will also be estimated for our model simulation so that a meaningful comparison between studies can be made. Also described are the quantile moments which are more robust to outliers than standard moments. These two moment measures will be compared to examine the affect of the outliers on the inferred results. These have not been used in other observational studies of vorticity.

The GEV distribution, which will be used to examine the maxima and minima of vorticity has also been defined. The nature of the symmetry between positive and negative extremes will be the primary use of this statistical tool.

Chapter 5

Exploratory Data Analysis

5.1 Introduction

Two numerical experiments are performed using the model described in Chapter 3 - firstly the two-dimensional turbulence case, with $\beta = 0$, and secondly the geostrophic turbulence case with $\beta > 0$.

5.1.1 Two-dimensional turbulence case

The $\beta = 0$ case is chosen to test the model without the extra complications of the differential rotation, and also allows comparisons with other numerical studies of two-dimensional turbulence. Physically, this situation represents turbulence on a cylindrical planet! In this situation, as $\beta = 0$, the potential vorticity (PV) is equal to the relative vorticity (RV). Fig. 5.1a shows a snapshot of the vorticity field after 500 days. It clearly shows the coherent vortices that form in the same way as previous numerical studies of two-dimensional turbulence (e.g. McWilliams 1990a). The differences between this study and previous two-dimensional turbulence models is that we are forcing the turbulence, and have included a zonal flow. The snapshot shows the vortices forming in the forcing region, and propogating along the domain.

The results presented here are from one particular set of initial conditions, and the sensitivity to these initial conditions is discussed in Section 5.5.

5.1.2 Geostrophic turbulence case

A more realistic (for the atmosphere) model would include the differential rotation of the planet (the β-effect) - and this case is analysed to see how the turbulent nature of the flow changes. A latitude of 45°N is chosen for the study, which is approximately where the 'storm track' exists on Earth, and this means that $\beta = 1.619 \times 10^{-11}\,\mathrm{s}^{-1}\,\mathrm{m}^{-1}$.
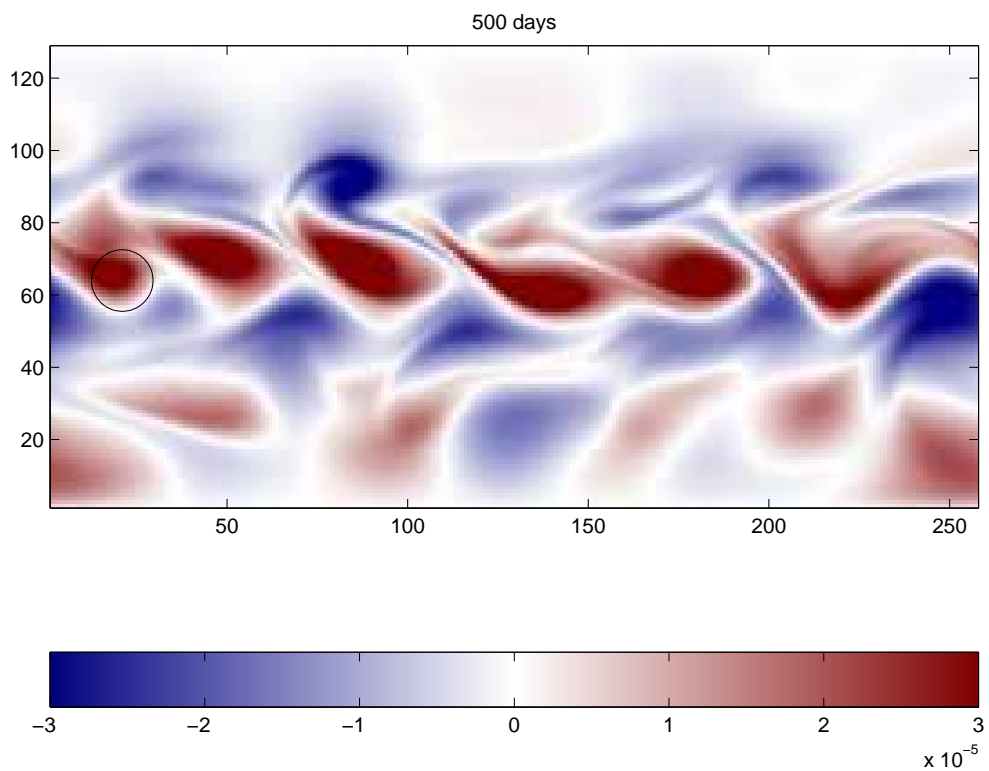
(a)
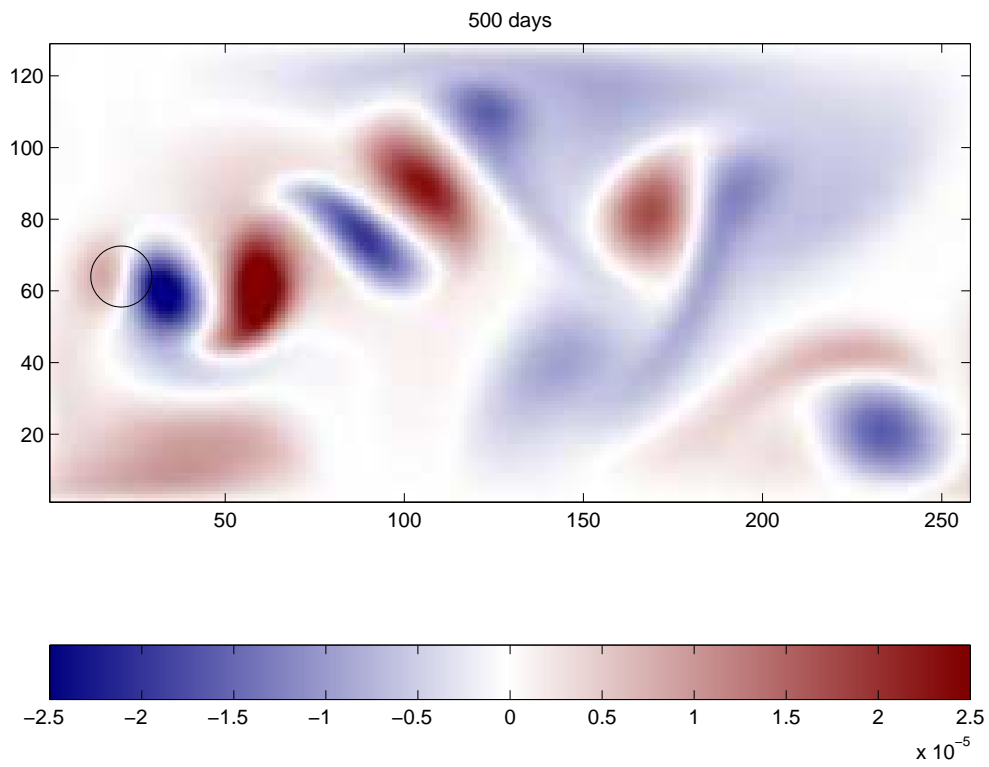
(b)

Figure 5.1: Snapshots of the relative vorticity field at $t = 500$ days for (a) $\beta = 0$, and (b) $\beta > 0$. The circle at the western end of the domain indicates the location of the forcing.

A snapshot of the relative vorticity is shown in Fig. 5.1b and it is clear that the two cases are strikingly different - the $\beta = 0$ case shows separated, coherent vortices at different latitudes, whereas the addition of β ensures the vortices are concentrated in a band, and are stretched and distorted. There are visual similarities between this figure and the 'storm track' itself which sees pressure systems propagating across the oceans. The scale of the vortices ($\sim 1000\,\mathrm{km}$) is also similar to the observed size of synoptic scale pressure systems.

5.2   Maps of the standard moments

The moments defined in Section 4.1 are calculated for both the $\beta = 0$ and $\beta > 0$ cases, using the data at every time-step, after the spin-up time. Appendix B.1 describes the estimation of an optimal spin-up time, and Appendix B.2 confirms why the data at every time-step must be used. Fig. 5.2 shows the mean and standard deviation of the relative vorticity for both cases, and Fig. 5.3 shows the skewness and kurtosis of the relative vorticity.

5.2.1   The mean vorticity

The plot of the mean of ξ in the $\beta = 0$ case (Fig. 5.2a) shows the formation of a vorticity gradient along the channel - this is the region where the mean vorticity is zero - although it is not positioned in the centre of the channel due to the presence of the forcing. Even in this simpler case the model has generated a gradient of vorticity which did not exist in the initial conditions.

In the geostrophic case (Fig. 5.2b), the plot clearly shows the formation of two 'jets' in the central latitudes, with a region of positive vorticity (low pressure systems) between two regions of negative vorticity. There is a weak third 'jet' at a more southerly latitude (at about 35 on the latitude grid point scale) where the sign of the mean vorticity changes again. The direction of these jets is the same as the structure observed in the atmosphere where the dominant wind pattern is with polar easterly winds, mid-latitude westerly winds, and the sub-tropical easterly trade winds. This structure, in the atmosphere, is caused by the Hadley cell circulation system, and the model has generated the same pattern.

5.2.2   The standard deviation of vorticity

The standard deviation in the $\beta = 0$ case (Fig. 5.2c) shows a turbulent wake caused by the forcing which is symmetrical about the forcing latitude. In the geostrophic model (Fig. 5.2d), the greatest variation in behaviour is directly downstream of the forcing, as expected. There is a more banded, latitudinal structure, due to the more confined nature of the turbulence, and it shows the simulated 'storm track' clearly.
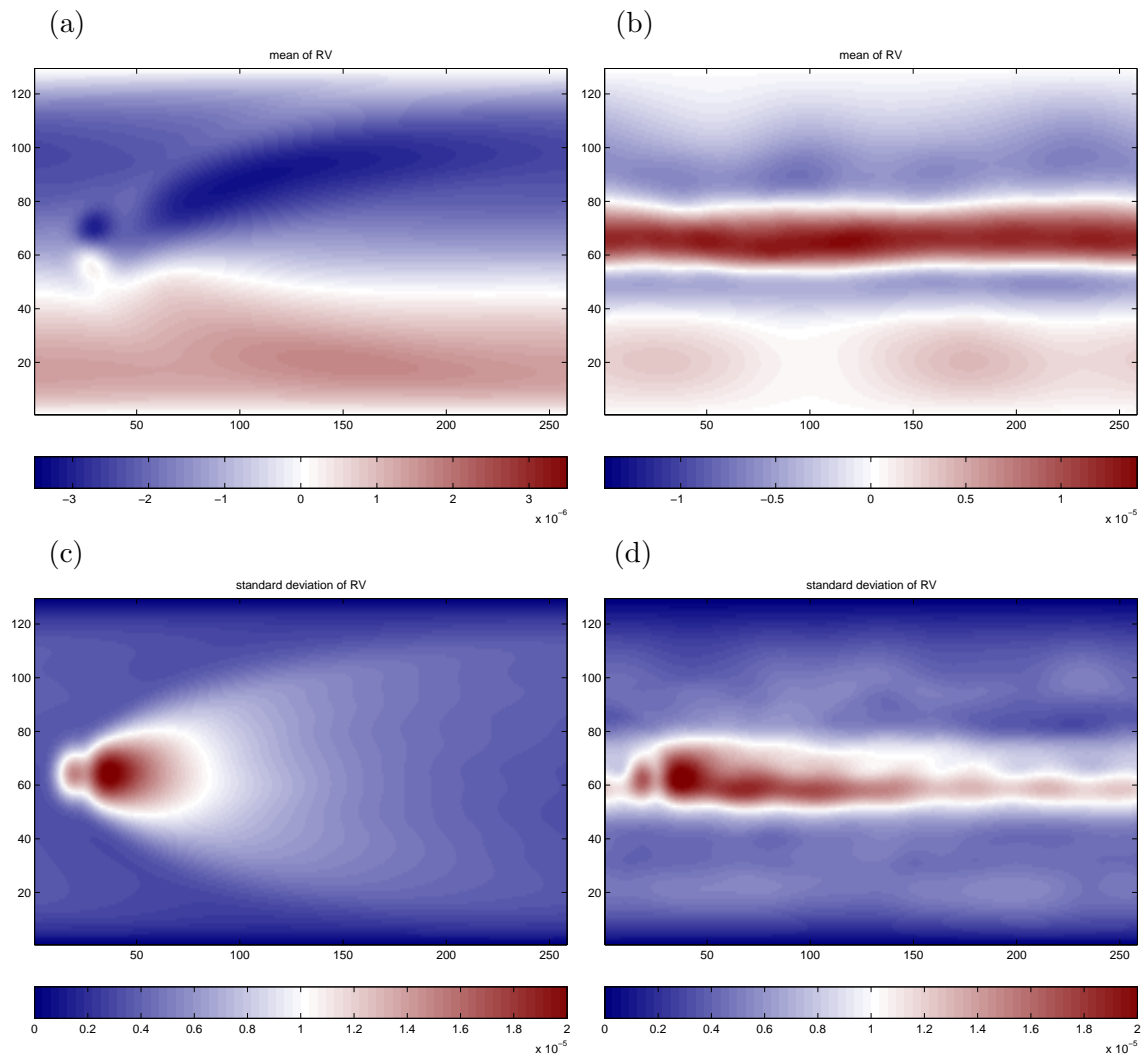
Figure 5.2: Mean relative vorticity for (a) $\beta = 0$, and (b) $\beta > 0$. Standard deviation of vorticity for (c) $\beta = 0$, and (d) $\beta > 0$. All panels use the data from every time-step.

5.2.3 The skewness and kurtosis of vorticity

The skewness in the two-dimensional turbulence case (Fig. 5.3a) is close to zero or negative away from the forcing effects, and there is a hint of a gradient of skewness with latitude, though this is not obvious away from the boundary of the domain. For the geostrophic version (Fig. 5.3b), the skewness contains various bands of alternating positive and negative skewness.

The kurtosis (b_2) in the $\beta = 0$ case (Fig. 5.3c) is larger than for a Gaussian distribution ($b_2 = 3$) for the vast majority of the channel, and is symmetric about the central latitude. The turbulent wake is again evident. When β is added to the simulation (Fig. 5.3d), the kurtosis decreases significantly over the vast majority of the domain. This is a commonly observed feature in previous numerical modelling studies (e.g. McWilliams 1990a, McWilliams 1990b) where the presence of a non-zero β stops the formation of coherent vortices, which cause the high kurtosis values seen.

Previous numerical studies (e.g. McWilliams 1984, Maltrud and Vallis 1991) have found that coherent vortices are a feature of two-dimensional turbulence. When averaged over the spatial domains in previous studies the coherent nature of the vortices produced large values of kurtosis. Here, we find large values of kurtosis at individual points when averaging over time. This suggests a degree of symmetry between the spatial and time dimensions and that each point sees a similar distribution of vortices.

Observations of the atmosphere indicate that skewness increases with latitude (White 1980, Swanson 2001) which is not clear here in either case. Interestingly the geostrophic turbulence map of kurtosis does approximately match the observations of White (1980) for the kurtosis, with larger than Gaussian values at high and low latitudes, and less than Gaussian in the mid-latitudes.

As is shown in Appendix B.1 the skewness and kurtosis are dominated by a few very extreme values in the numerical model. Nakamura and Wallace (1991) noted that this was also true in observations of the atmosphere. This suggests that they are not the best measures to use, and that care must be taken when interpreting the results. The alternative, quantile form of the moment estimates are considered in the next section.
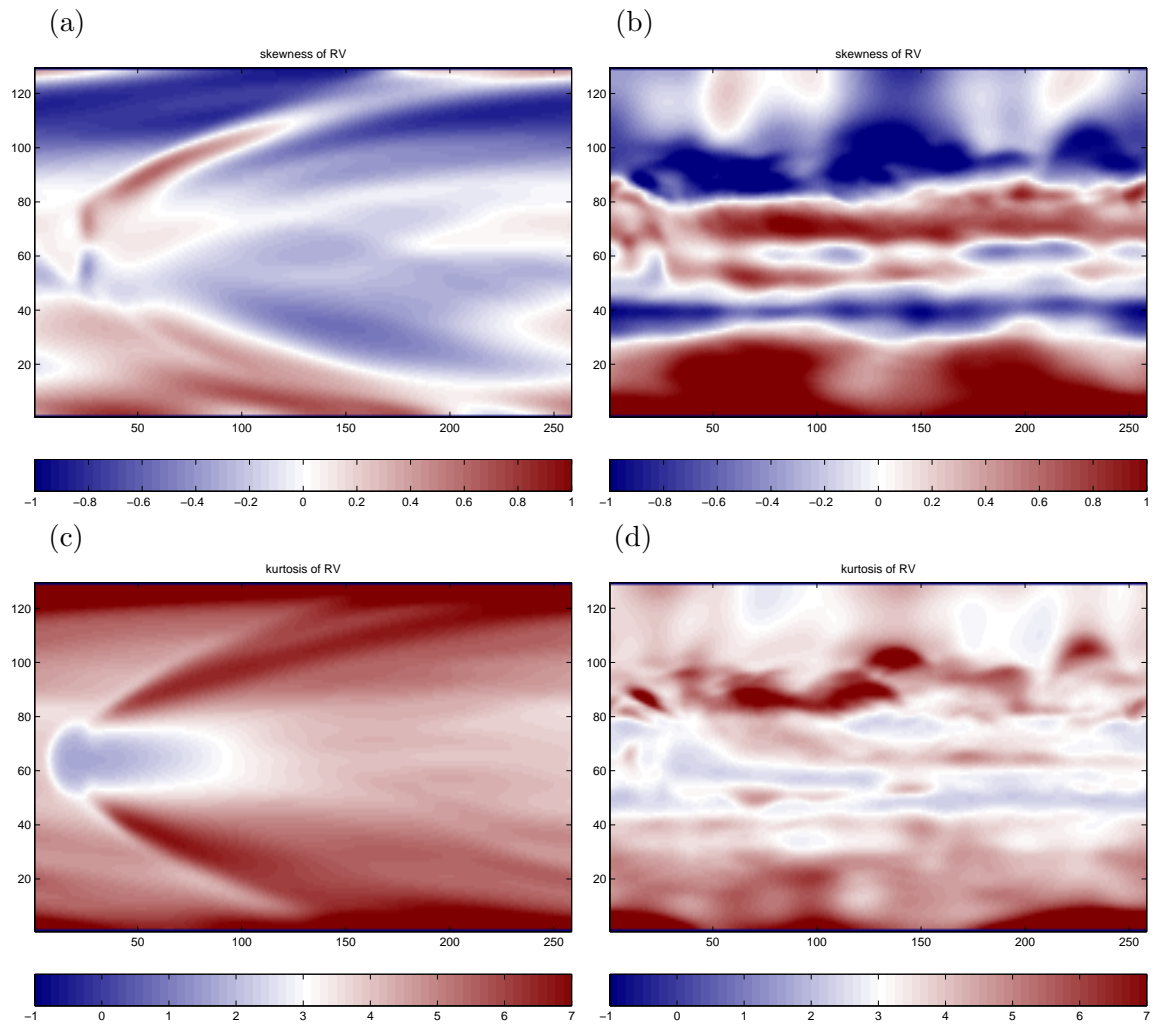
Figure 5.3: Skewness of vorticity for (a) $\beta = 0$, and (b) $\beta > 0$. Kurtosis of vorticity for (c) $\beta = 0$, and (d) $\beta > 0$. All panels use the data from every time-step.

5.3 Latitude cross-section

The maps presented do not provide an easy way of examining any trends in latitude. So, we now consider a band of latitude at a single longitude point ($x = 200$), downstream from the forcing.

5.3.1 Latitude-time cross-section

Fig. 5.4 shows a time lapse plot of the vorticity on this cross-section with time, in 10 time slices from $t = 0$ to $t = 1000$ days, with 100 days in each row for the $\beta = 0$ case, and Fig. 5.5 shows the same for the $\beta > 0$ case.

The time for the random nature of the initial conditions to be come more structured is clearly short in both figures, and it is seemingly settled after the first $100 - 300$ days (also see Appendix B.1).

It is striking, though, that there seem to be various regimes during the 1000 days. In the $\beta = 0$ case the vortices become more extreme for a period around 550 days and less extreme at around 700 days. There is an impression that negative vorticity becomes more dominant at later times.

The geostrophic time-lapse plot also seems to show a range of different regimes - with very regular periods ($100 - 400$ days) punctuated by more turbulent periods ($450 - 700$ days), and quieter periods ($700 - 1000$ days). This makes the analysis of this run more complicated as the statistical measures, such as the mean, may not be stationary.

5.3.2 Standard and quantile moment comparisons

Fig. 5.6 shows comparisons for the standard moments and the quantile moments calculated along this latitude cross-section for the two-dimensional turbulence experiment. Note that the scales are different for each panel. Although the quantile measures seem more noisy this is partly due to the expanded scale for the standard moments, i.e. the variation between grid points relative to the variation over all latitudes is greater for the quantile moments. Fig. 5.7 shows the same for the geostrophic turbulence experiment.

For the two-dimensional case the mean and median curves are very similar and both show the zero vorticity point at a latitude below the centre of the domain. This is the non-centred 'jet' seen previously in the maps. In the geostrophic plots, the triple 'jet' structure can be seen, and the two measures are again similar.

The standard deviation and inter-quartile range plots show the same shape with very little variation with latitude in the two-dimensional case, apart from in the boundary regions. This is markedly different to the geostrophic case where the standard deviation is significantly larger in the central latitudes where the turbulence is confined.
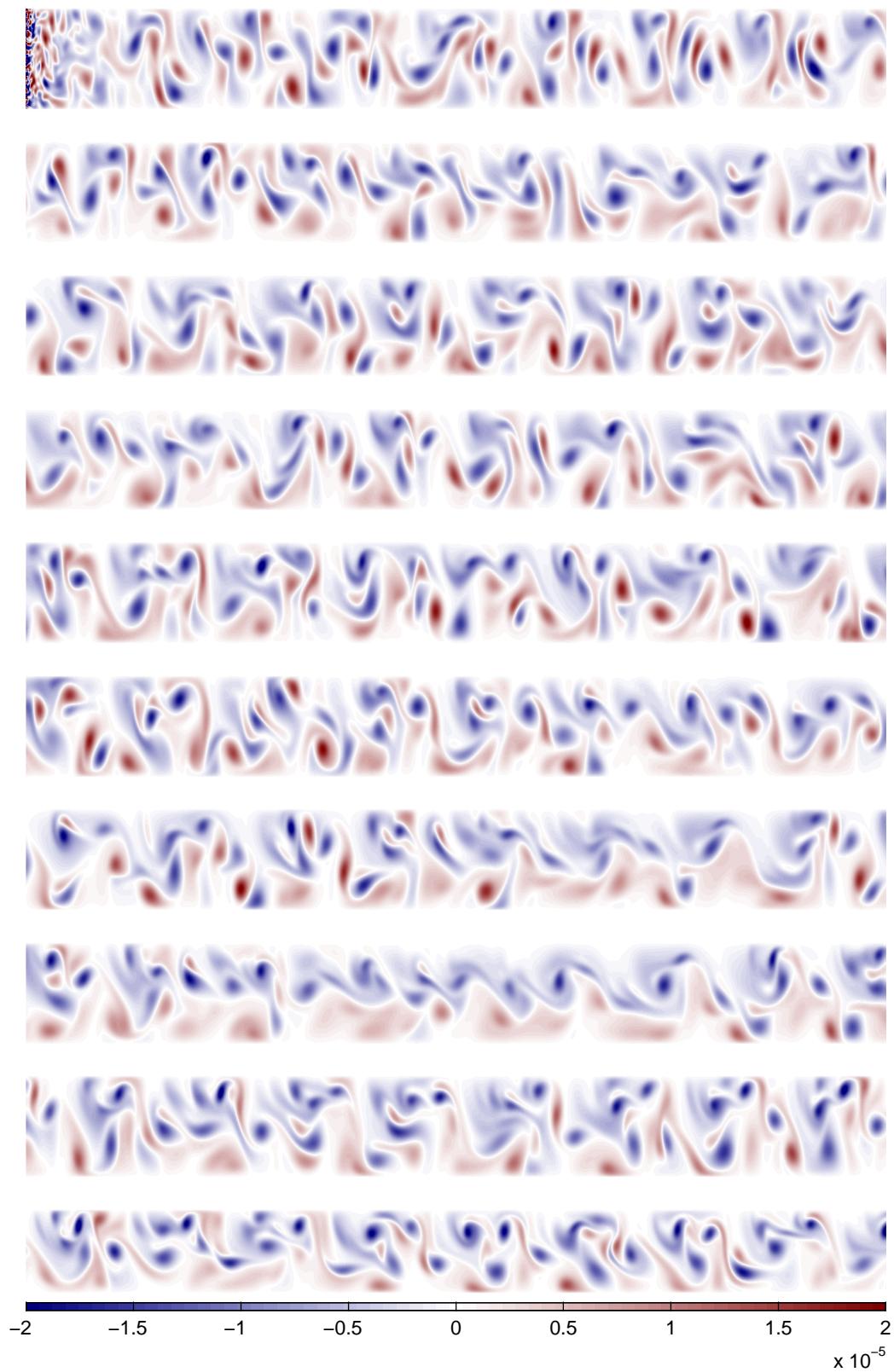
Figure 5.4: Latitude-time cross section of relative vorticity for $\beta = 0$ in 100 day slices, starting at $t = 0$.
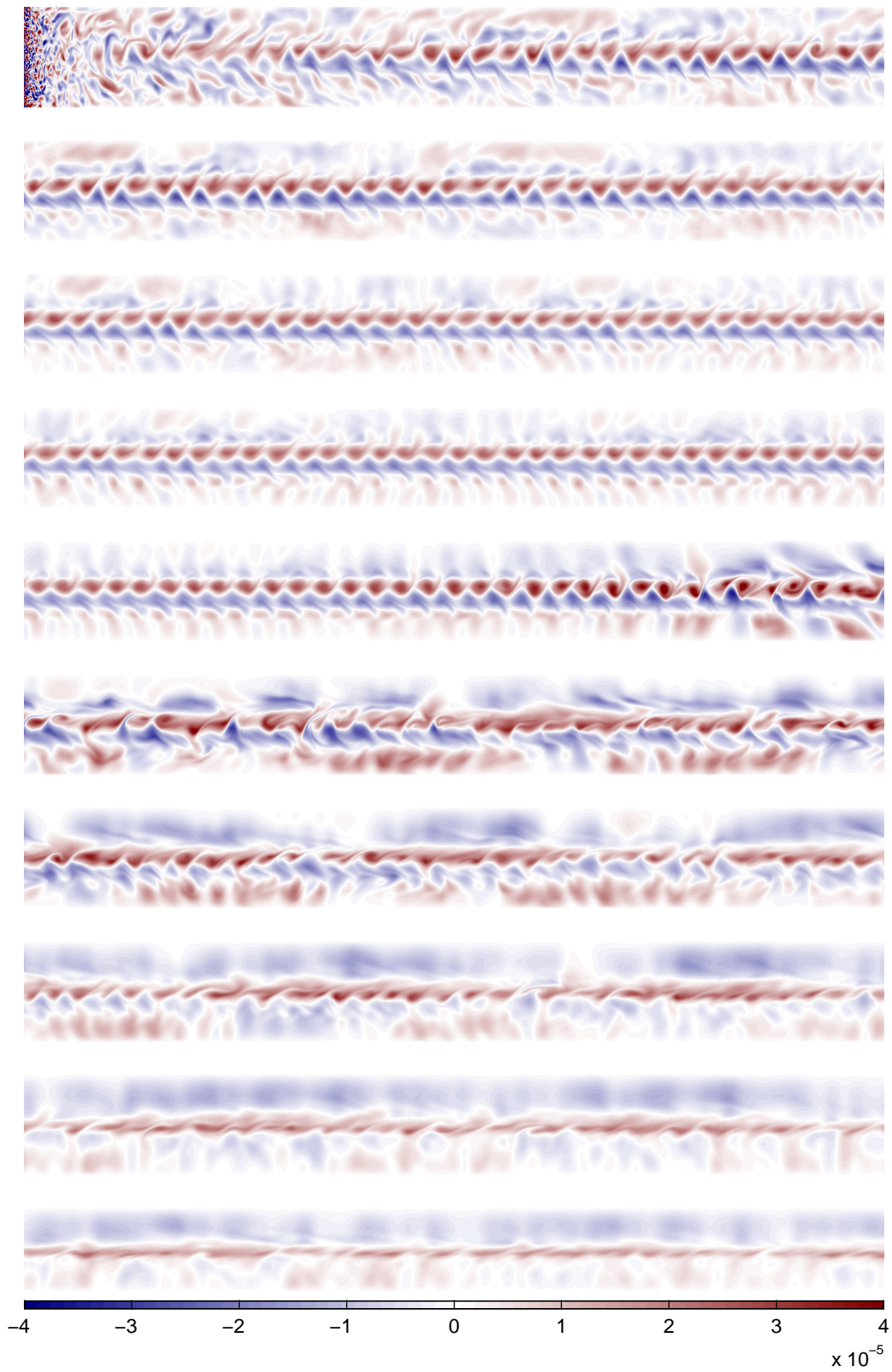
Figure 5.5: Latitude-time cross section of relative vorticity for $\beta > 0$ in 100 day slices, starting at $t = 0$.
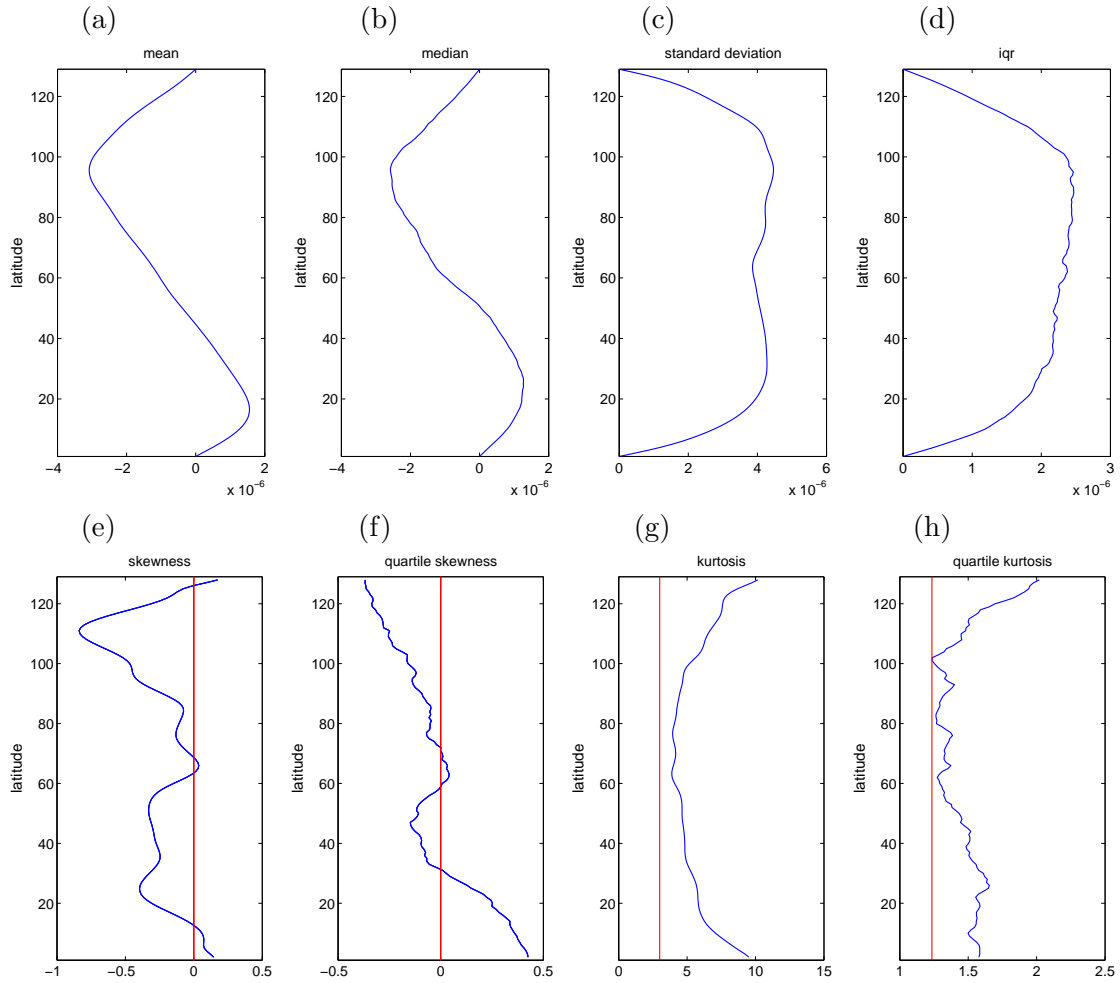
Figure 5.6: Comparisons of the first four moments of relative vorticity, with their respective quantile moments for two-dimensional turbulence - (a) mean, (b) median, (c) standard deviation, (d) inter-quartile range, (e) skewness, (f) quartile skewness, (g) kurtosis, and (h) quartile kurtosis. The red lines are the Gaussian values for the higher order moments.

The skewness plots for the $\beta = 0$ case show a decrease of skewness with latitude, and this is larger in the quantile measure. There is a dominance of negative skewness. As stated previously both White (1980) and Swanson (2001) found an increase of skewness with latitude - the opposite of what we see here. In the geostrophic version there is an increase of skewness, if only the central latitudes $(40 - 80)$ are examined, but this is less clear in the quantile skewness. This central region is where the β-plane approximation works best and is around $40°$ of latitude, and is where the model should be compared with the observations.

Both kurtosis panels for the $\beta = 0$ version clearly show that the measures give values larger than for a Gaussian distribution ($b_2 = 3$, quantile kurtosis = 1.235) throughout the channel. In the geostrophic case the kurtosis is much more similar to the values for
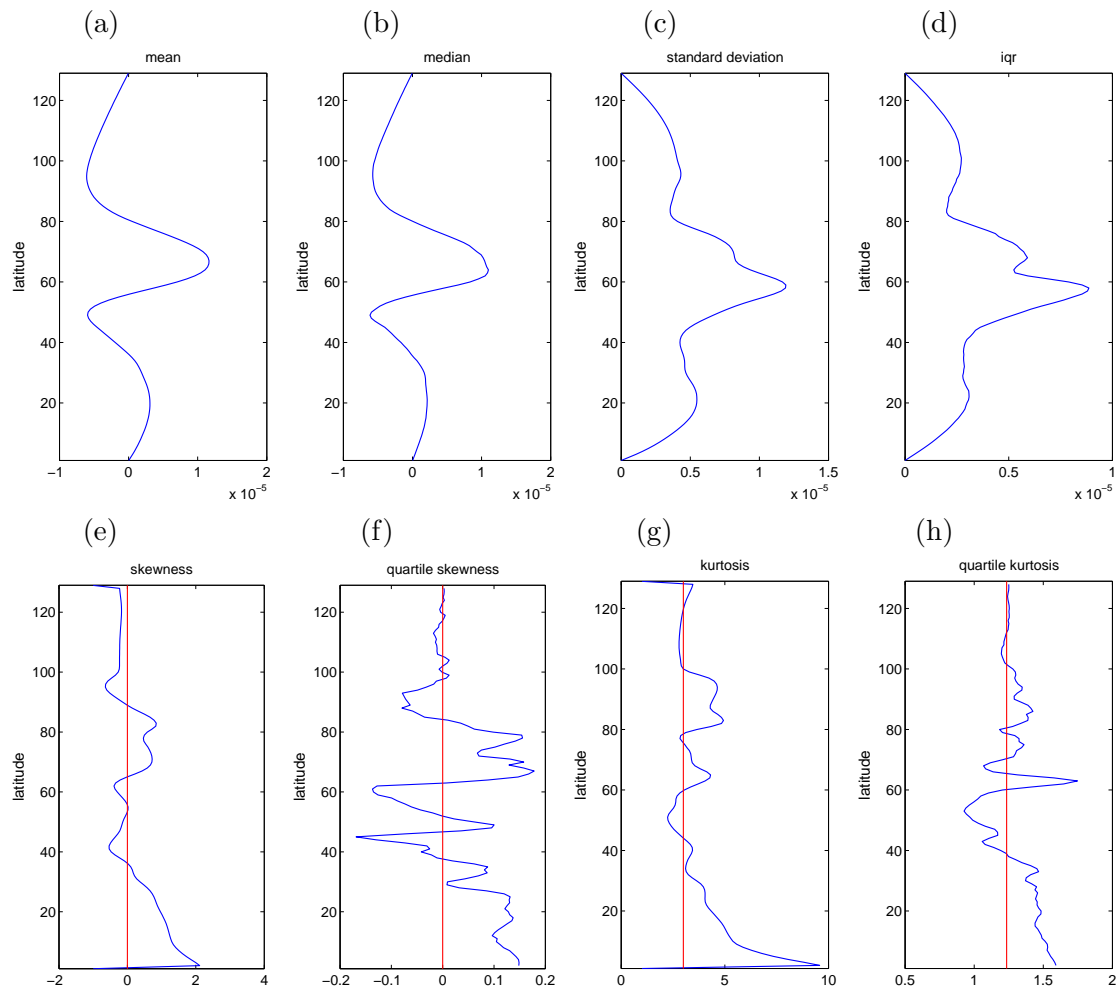
Figure 5.7: Comparisons of the first four moments of relative vorticity, with their respective quantile moments for geostrophic turbulence - (a) mean, (b) median, (c) standard deviation, (d) inter-quartile range, (e) skewness, (f) quartile skewness, (g) kurtosis, and (h) quartile kurtosis. The red lines are the Gaussian values for the higher order moments.

a Gaussian distribution as already seen in the maps, and there is too much variation to compare to the observations of White (1980).

It has been seen that the two different moment estimates give very similar results. The quantile form is more resistant to extreme outliers, but is more noisy in this case.

5.4   Time series and histogram

Fig. 5.8a shows the time series of vorticity for a specific point ($x = 200, y = 64$ - i.e. in the centre of the channel) using data from every time-step in the $\beta = 0$ case. The 'quieter' period visible in the time-lapse figure is easily picked out in the time series plot as a sudden reduction in variance around $650 - 800$ days. Fig. 5.8b shows the time series at the same point for the geostrophic version. The features seen in the time lapse figure can be seen in the time series - with regular oscillating vorticity near the start, followed by a more turbulent period, and then becoming quieter towards the end.

Fig. 5.9 shows the histograms for the same point. In the $\beta = 0$ case, the histogram has a slight asymmetry with a few extreme values in the tails - heavier than the Gaussian distribution shown. This is one of the most Gaussian-like points in the band. In the geostrophic case, there is evidence for a double peak - due to the regular relative vorticity periods alternating between slightly positive and slightly negative. This is a bimodal distribution, which was also observed for PV in the atmosphere by Swanson (2001).

## 5.5   Sensitivity to initial conditions

On running the two-dimensional turbulence case again with different sets of random initial conditions it was found that the calculated moments changed - this is a property known as 'non-ergodicity'. Fig. 5.10 shows the mean of potential vorticity from four sets of initial conditions. Each figure shows a gradient of vorticity with the zero vorticity 'jet' in different places, with Fig. 5.10b showing the opposite of the results presented above, with positive vorticity dominating, and Figs. 5.10c,d show a much more even spread of vorticity.

These results indicate that a larger ensemble of runs is required to analyse how this situation arises. It would also be interesting to do longer simulations to examine whether the turbulence tends to stay in one fixed state, or whether it can switch between different stable states, i.e. whether the turbulence is 'intransitive' (Lorenz 1970).

The skewness moments were also changed by this initial condition dependence - if positive vorticity dominates then the skewness is more positive (and vice versa), and if there is no dominant vorticity then the skewness is close to zero over much of the domain (not shown).

The variation of mean vorticity was not reflected in the variance, which remained the same, and kurtosis, which remained much higher than for a Gaussian distribution over most of the domain - the maps (not shown) all look very similar to Fig. 5.3c.
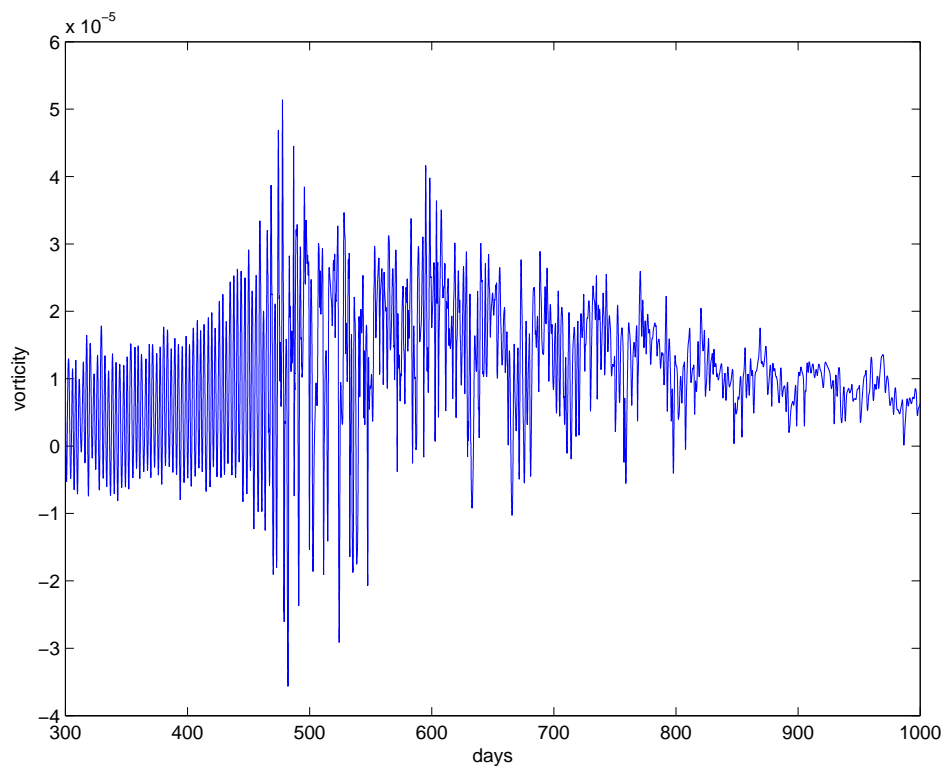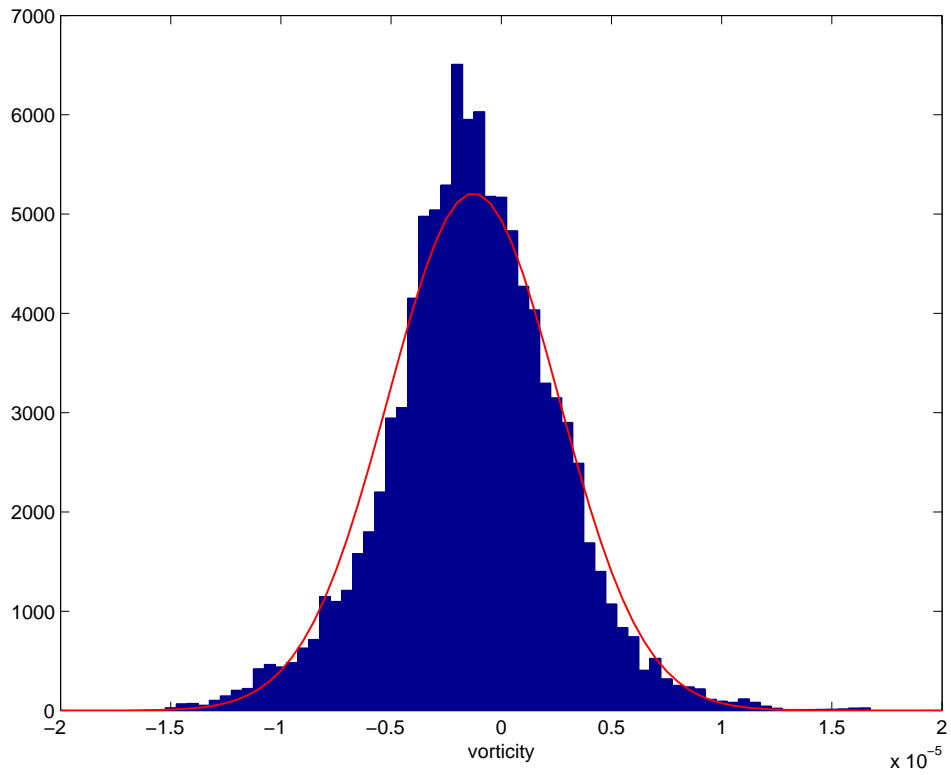
(a)
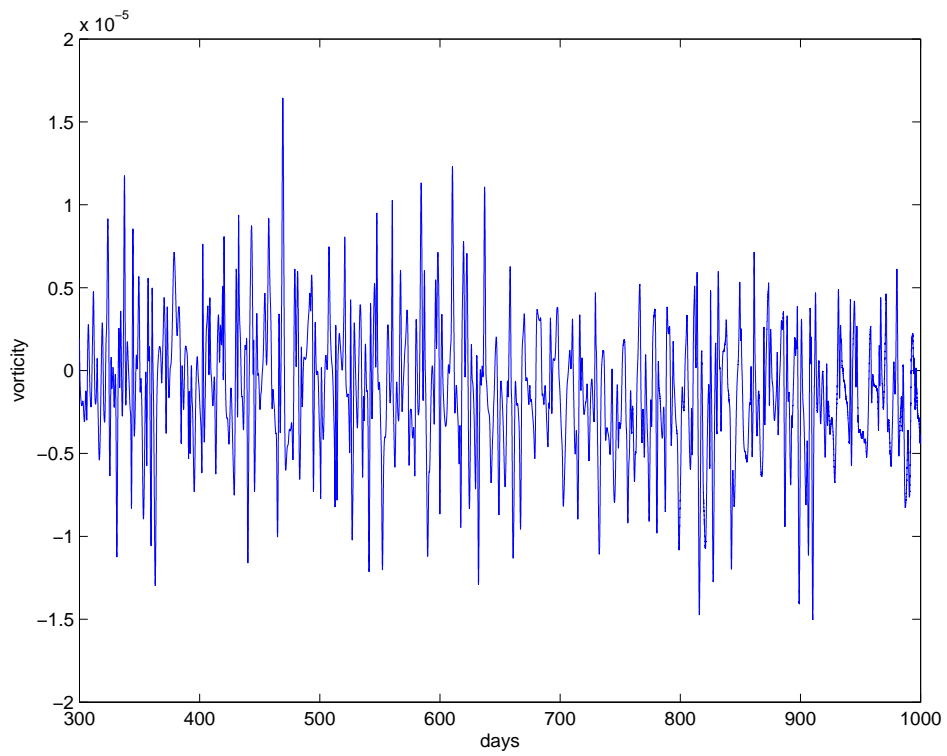
(b)

Figure 5.8: Time series of vorticity at a single point after the spin-up time for (a) $\beta = 0$, and (b) $\beta > 0$.
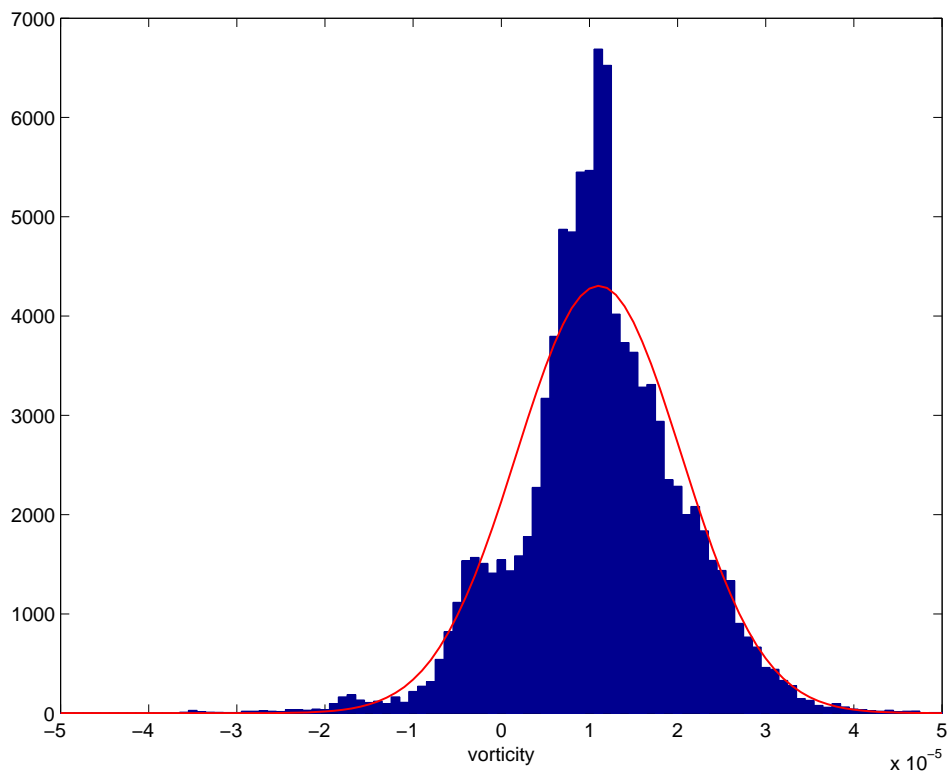
(a)

(b)

Figure 5.9: Histogram of potential vorticity at a single point after the spin-up time for (a) $\beta = 0$, and (b) $\beta > 0$. The red line is the Gaussian distribution with the same mean and standard deviation as the corresponding time series.
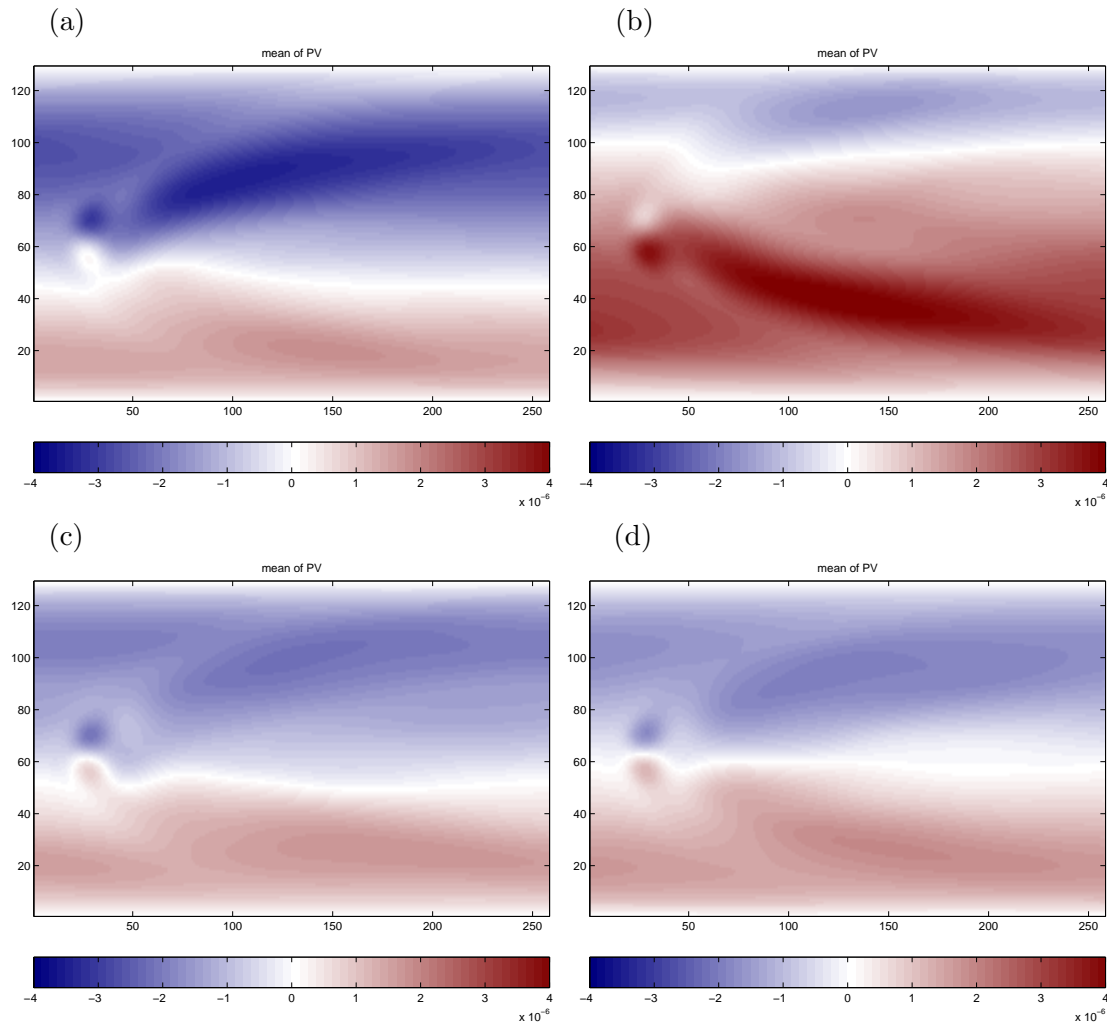
Figure 5.10: Mean of potential vorticity for (a) the results presented above, and (b), (c), and (d) for different random initial conditions.

5.6   Summary

The moments of the simulated geostrophic turbulence have been shown to produce maps of the mean, skewness and kurtosis which are all qualitatively similar to the atmosphere. The differences between the kurtosis maps for geostrophic and two-dimensional turbulence are consistent with what has been seen in previous numerical studies.

The dependence on initial conditions, and existence of various regimes in both types of turbulence suggests that an ensemble of longer simulations are required to examine each of these effects in more detail.

Chapter 6

Extremes of Vorticity in Turbulence

6.1 Introduction

The main aim for this project was to examine the extremes of both positive and negative potential vorticity in the numerical model. The symmetry and latitude dependence of the extremes will be the main focus of this chapter. The statistical methodology that will be used was described in Section 4.3.

To estimate the maxima and minima, a suitable block size (see Section 4.3.2) needs to be determined. It is found that, for this model, a 10-day block size is optimal for both extreme positive and negative vorticity, and this is shown in Appendix B.3.

6.1.1 Verification tests

Once a suitable block size is chosen it needs to be confirmed that the GEV distribution is actually a good fit to the data. The plots for doing this were described in Section 4.3.4. Fig. 6.1 show three different types of plot to test the model fit for a single point for the block maxima (i.e. positive potential vorticity), and these are typical of the points in the latitude band away from the boundary. The left column is for the $\beta = 0$ experiment and the right column for the geostrophic case. They all show that the data fits the model distribution well, i.e. the data points lie near the line in each case. Fig. 6.2 shows the same for the block minima (i.e. negative potential vorticity) and again the GEV distribution is a good fit to the data.
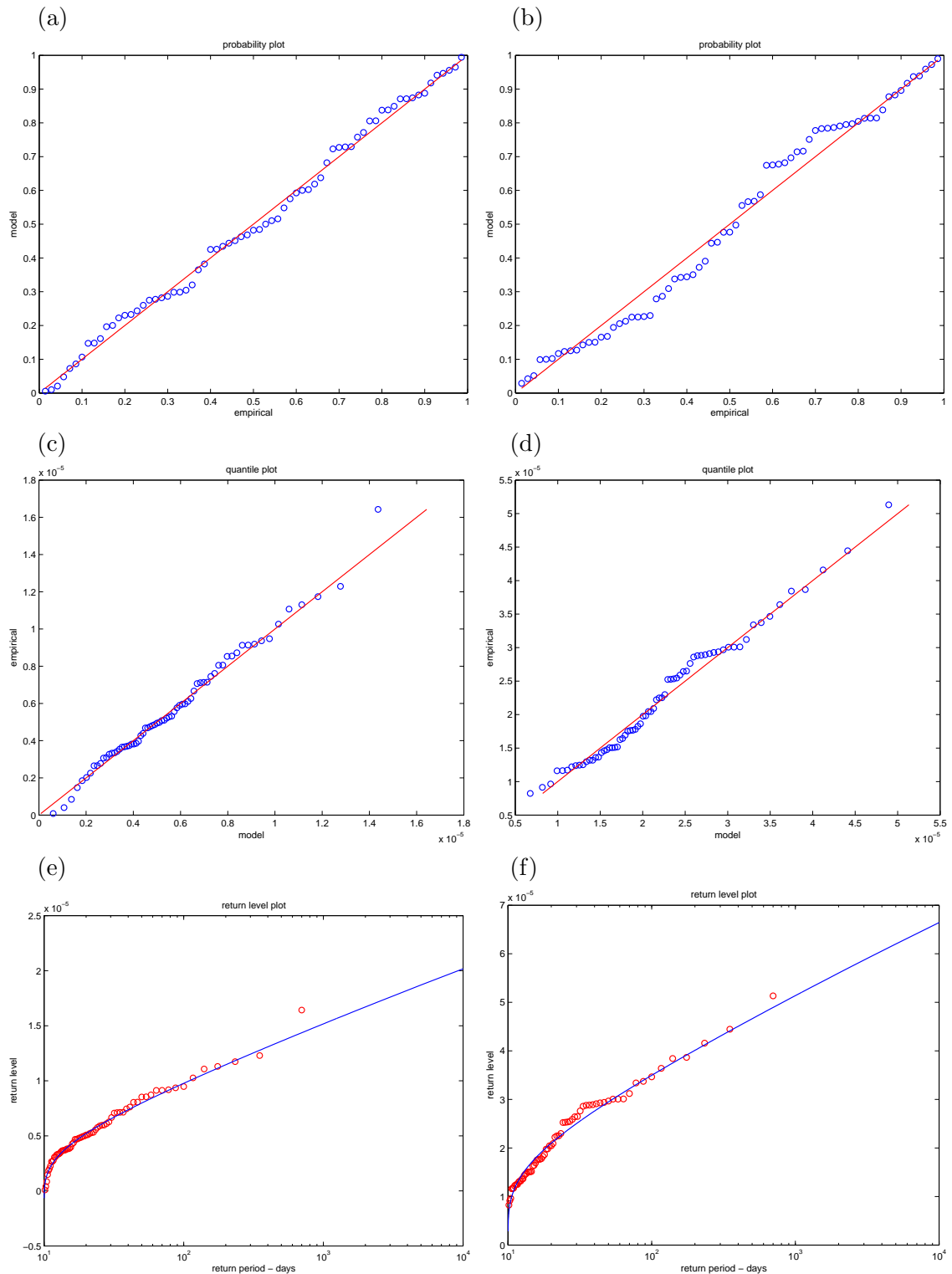
Figure 6.1: Tests on the distributions of maxima for a typical single point in a latitude band. Probability plots for (a) $\beta = 0$, and (b) $\beta > 0$. Quantile plots for (c) $\beta = 0$, and (d) $\beta > 0$. Return level plots for (e) $\beta = 0$, and (f) $\beta > 0$. Circles are the data, and the lines are the model distributions.
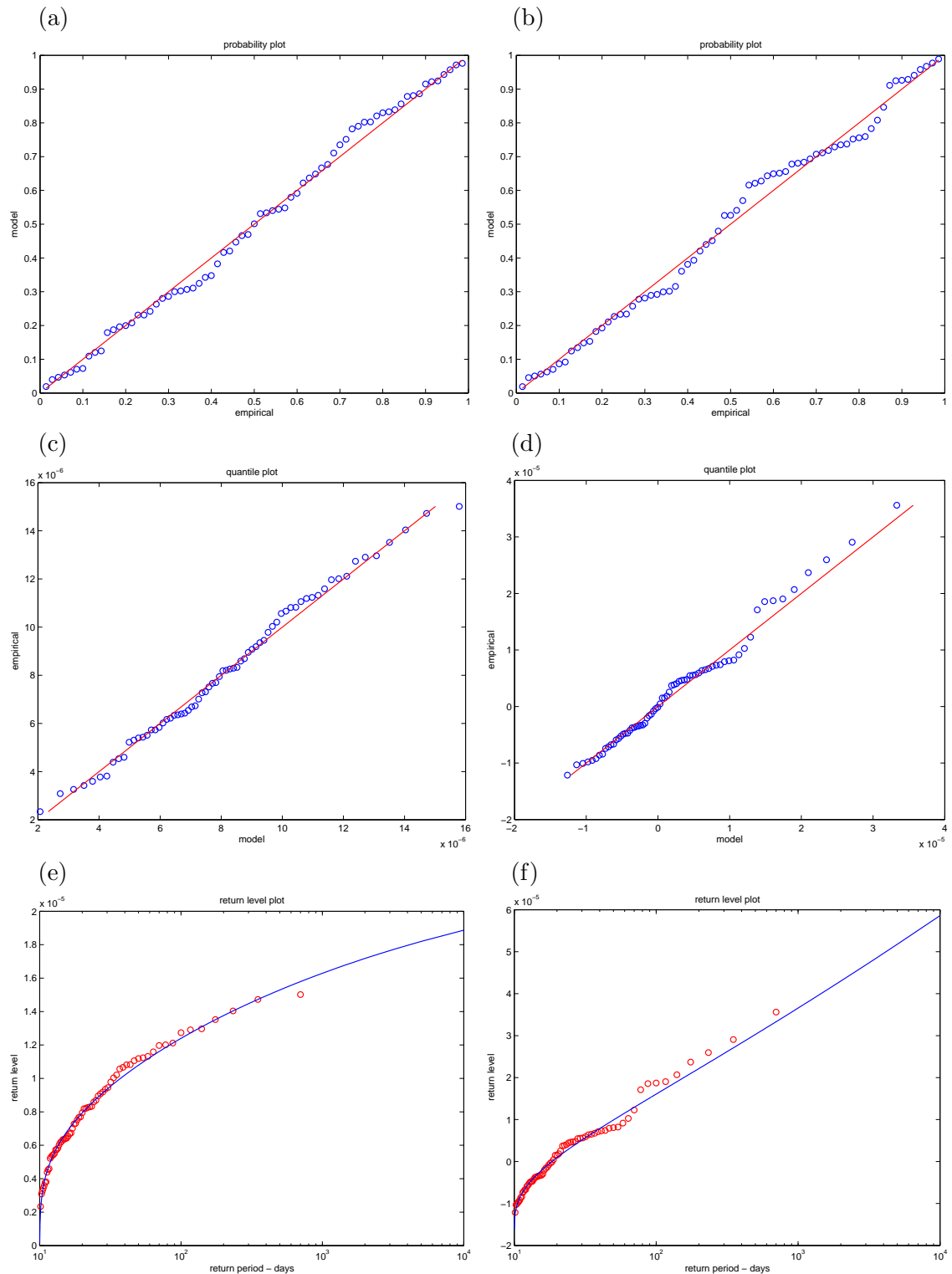
Figure 6.2: Tests on the distributions of minima for a typical single point in a latitude band. Probability plots for (a) $\beta = 0$, and (b) $\beta > 0$. Quantile plots for (c) $\beta = 0$, and (d) $\beta > 0$. Return level plots for (e) $\beta = 0$, and (f) $\beta > 0$. Circles are the data, and the lines are the model distributions.

6.2 Latitude variation of vorticity extremes

After verifying that the GEV distribution is a good fit to the data we can start to examine the estimated distribution parameters in more detail. Fig. 6.3 shows the variation of the GEV distribution shape parameter ($\hat{\gamma}$) and confidence intervals as a function of latitude grid points, for both maxima and minima, and for both numerical experiments. The blue line (when shown) is the maximum likelihood estimate (Eqn. 4.3), the solid red line is the closed form estimate (Eqn. 4.4), with dashed red lines giving the 95% confidence intervals. The maximum likelihood estimate had trouble converging in the geostrophic case, and is not shown. The two different estimates are consistent in the $\beta = 0$ case, apart from the boundary regions, where it is seen (not shown) that the distribution is not well fitted by
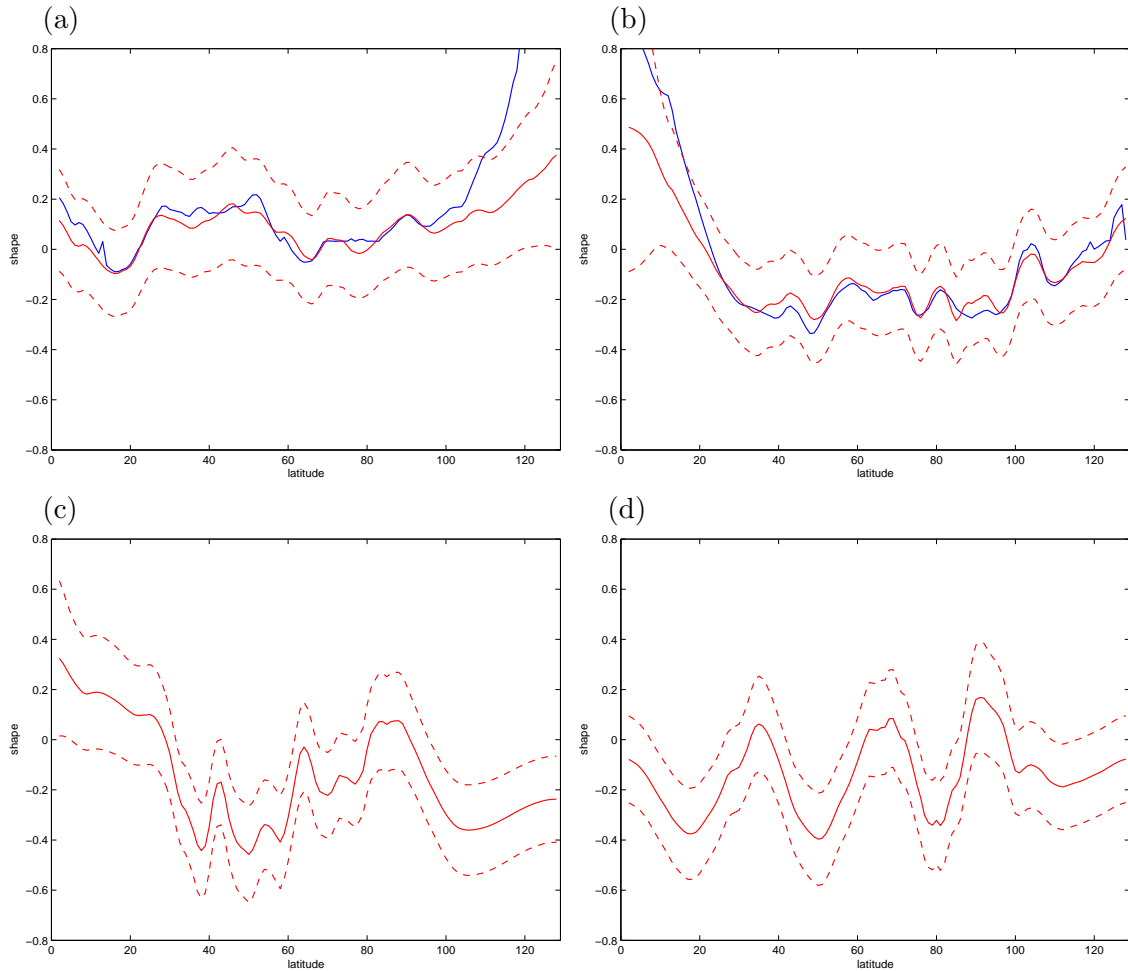

Figure 6.3: Latitude variation of estimated GEV distribution shape parameter, $\hat{\gamma}$ - (a) maxima for $\beta = 0$, (b) minima for $\beta = 0$, (c) maxima for $\beta > 0$, and (d) minima for $\beta > 0$. The red line is the closed-form estimate with dashed 95% confidence intervals, and the blue line (when shown) is the maximum likelihood estimate.

a GEV distribution. This is likely to be due to boundary effects, and the grid points near the boundary should be ignored.

It can be seen that the estimated shape parameters are consistent with no dependence on latitude in the $\beta = 0$ experiment. The shape parameter is slightly positive for the positive vorticity extremes, but consistent with zero for the entire central region, and the errors are approximately ± 0.15. For the minima the shape parameter is significantly negative over the whole range, rather than zero, suggesting that the minima and maxima have slightly different GEV distribution shapes.

The negative shape parameter for the negative vorticity extremes (high-pressure systems) implies that these systems have a finite bound, whereas the positive vorticity extremes (low-pressure systems) have a shape parameter consistent with zero which implies that infinite values of vorticity can occur. The fact that the distributions are not exactly symmetrical and the broad agreement with the observations (Venn 1887, also see Section 2.2) that high pressure systems are not so extreme is a surprising result in this two-dimensional turbulence. It must be noted that the significance of this feature is not high.

In the geostrophic case the shape parameter is negative over most of the domain for both maxima and minima, with some oscillations, especially in the negative vorticity (minima) figure. In this experiment the distributions are more symmetric, but these intriguing oscillations suggest that certain latitudes can experience different extremes.

Fig. 6.4 shows the variation of the GEV distribution scale parameter ($\hat{\sigma}$) and confidence intervals as a function of latitude grid points, for both maxima and minima, and for both numerical experiments. In the two-dimensional experiment the scale parameter is consistent with being a constant over the domain away from the boundary, though there is a possible dip in the central regions. This is consistent with the result that there is a slight decrease of standard deviation for the whole vorticity distribution in the central part of the domain.

Fig. 6.5 shows the variation of the GEV distribution location parameter ($\hat{\mu}$) with latitude - and they show striking trends. In the two-dimensional turbulence case these trends are entirely consistent with the fact that the mean potential vorticity decreases with latitude. Hence, when examining maxima it would be expected to see a decrease in the location, and when considering minima it would be expected to see an increase, remembering that we are using the negative of the block minima, for which a larger location parameter implies a more negative location.

In the geostrophic case, the potential vorticity gradient is reversed and larger than the two-dimensional case, and so the location parameter trends are also reversed.

In summary, the results for the scale and location parameters are consistent with what has been seen in the mean vorticity plots, and it is the shape parameter which has provided some extra new information.
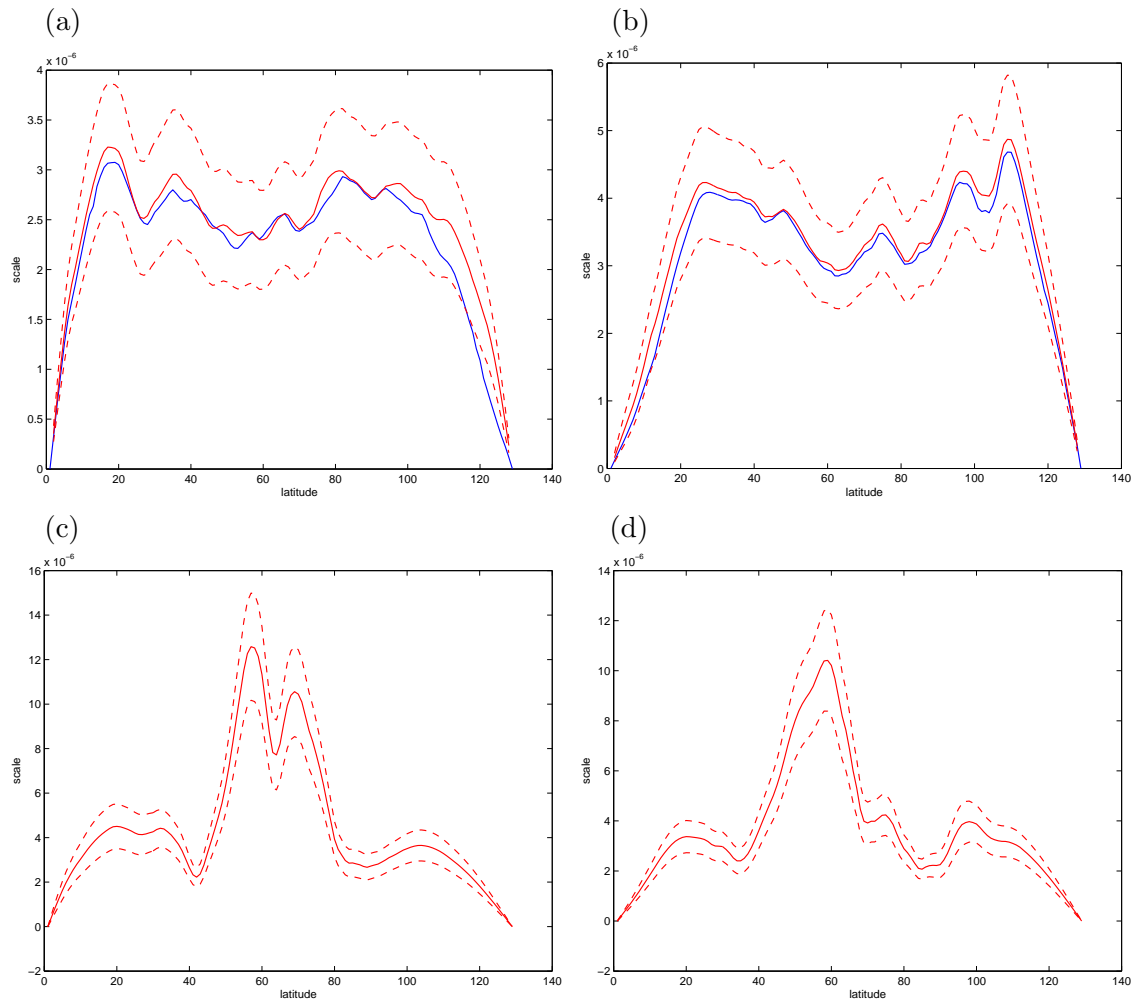
Figure 6.4: Latitude variation of estimated GEV distribution scale parameter, $\hat{\sigma}$ - (a) maxima for $\beta = 0$, (b) minima for $\beta = 0$, (c) maxima for $\beta > 0$, and (d) minima for $\beta > 0$. The red line is the closed-form estimate with dashed 95% confidence intervals, and the blue line (when shown) is the maximum likelihood estimate.

Figure 6.5: Latitude variation of estimated GEV distribution location parameter, μ - (a) maxima for $\beta = 0$, (b) minima for $\beta = 0$, (c) maxima for $\beta > 0$, and (d) minima for $\beta > 0$. The red line is the closed-form estimate with dashed 95% confidence intervals, and the blue line (when shown) is the maximum likelihood estimate.
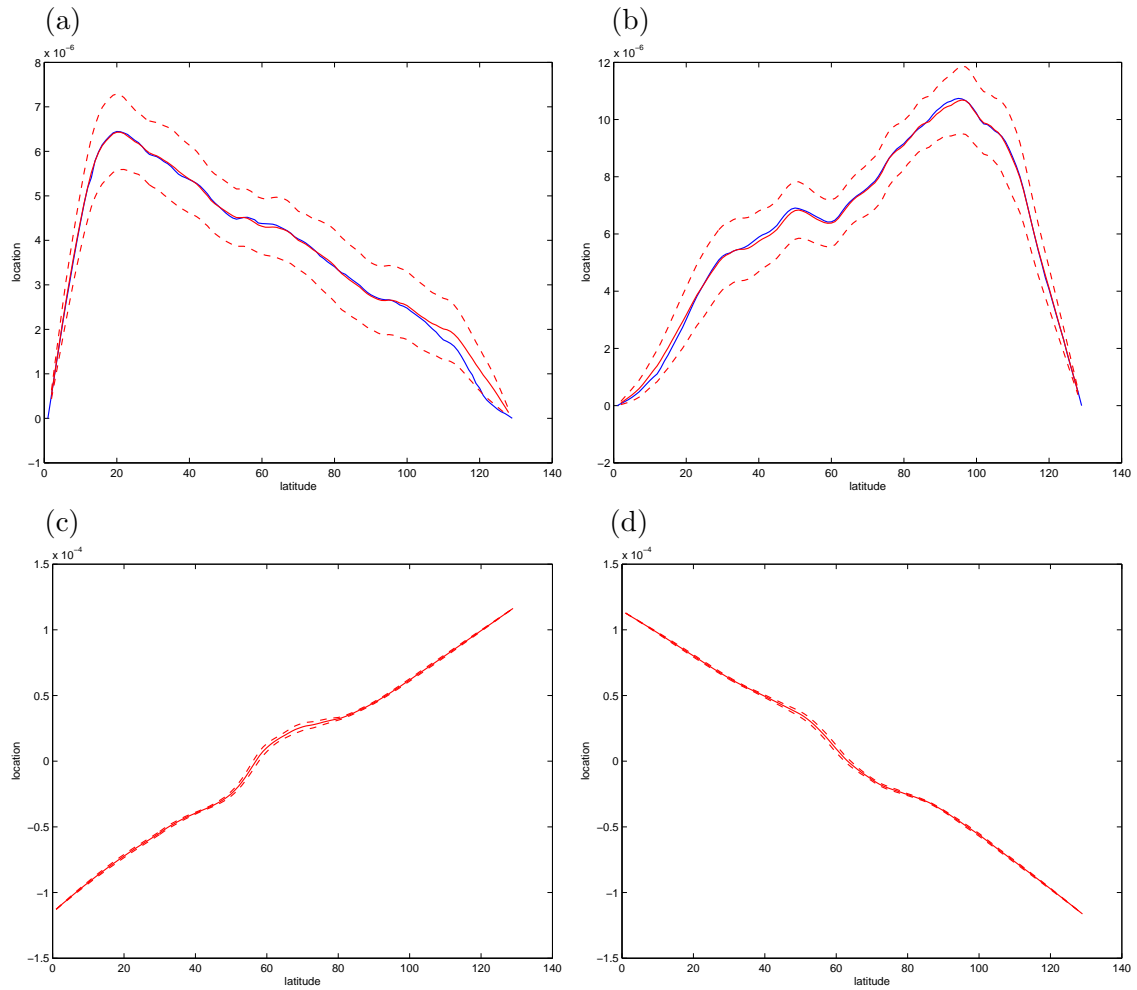
6.3   Maps of vorticity extremes

Rather than look at a cross-section, it is possible to see how the parameters vary as a function of latitude and longitude. Fig. 6.6 shows the GEV distribution shape parameters as a map, using the closed form estimate of the parameters, as this is quicker to calculate and has been shown to be consistent with the maximum likelihood form.

The shape parameter for the two-dimensional turbulence case again shows the turbulent wake seen in the moment analysis, and also the strong asymmetry in shape parameter between maxima and minima that has already been noted in the latitude cross-section. The map of maxima is consistent with zero for much of the domain (errors are about ± 0.15), whereas in the minima map, in most non-boundary regions, the value of $\hat{\gamma}$ is negative, though in many areas the value is not significantly non-zero. Remembering that
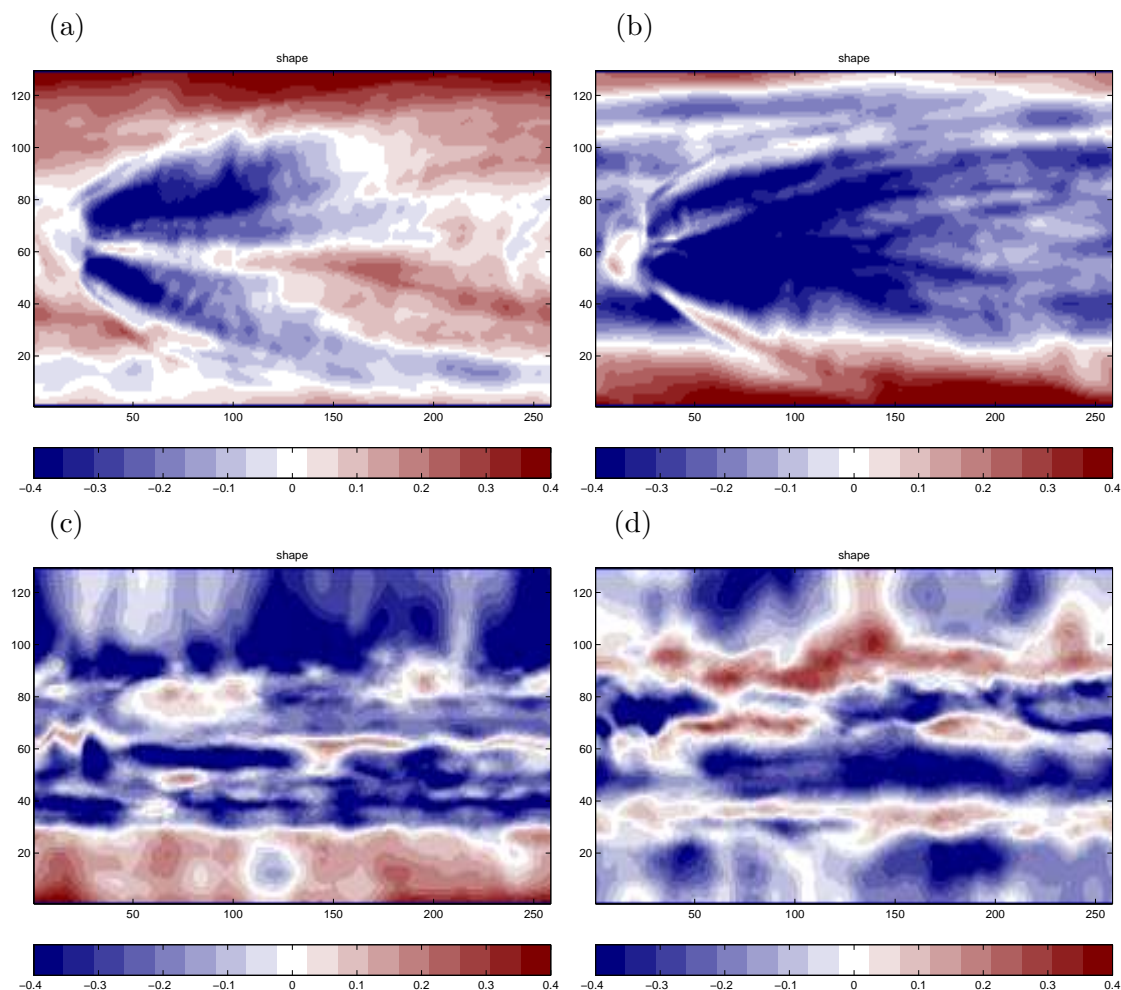

Figure 6.6: Maps of the estimated GEV distribution shape parameter, $\hat{\gamma}$ - (a) maxima for $\beta = 0$, (b) minima for $\beta = 0$, (c) maxima for $\beta > 0$, and (d) minima for $\beta > 0$.

a negative shape parameter has a sharp cut-off to the distribution (Eqn. 4.2), the minima map shows that the negative vorticity (high-pressure systems) has a finite bound, whereas the positive vorticity (low-pressure systems) has an infinite bound over a large area. This again agrees with the observations of Venn (1887).

When β is added to the model simulation (Fig. 6.6c,d), the maps of the shape parameter change significantly, now showing a banded structure, as was seen in the latitude cross-section. In the maxima map, the shape parameter is predominantly negative away from the boundary regions, and although the same is true for the minima, there are more regions of positive shape. When considering the errors of about ± 0.15 on the shape parameter at each grid point, these differences are not very significant.

Fig. 6.7 shows the GEV distribution scale parameter, $\hat{\sigma}$ for both simulations. It is instantly clear that there is little difference between the maxima and minima maps for each simulation. The $\beta = 0$ case shows the turbulent wake clearly again, and the geostrophic version shows the 'storm track' confined to the central latitudes. There are hints of a double band of scale, especially in the maxima (positive vorticity) map.

The maps of location parameter are shown in Fig. 6.8. In the two-dimensional case the maps are dominated by large values near the forcing, and this is imposed on the gradient in location parameter which is seen further downstream. There is a similarity between this map and the standard deviation moment map near the forcing, which is intriguing. In the geostrophic case, the location parameter is dominated by the gradient of potential vorticity as expected.

There is a fourth parameter that is interesting to examine - z_+ (see Eqn. 4.2) - the cutoff value of vorticity. This can only be plotted for the regions where the shape parameter is negative, as it has an infinite value in all other areas. Any variation in this parameter would indicate some regions being able to experience different extreme vorticity - and Fig. 6.9 shows this parameter - the white regions are where there is an infinite upper bound. For the two-dimensional case the upper cutoff, if it exists, shows little variation with latitude over the domain. The geostrophic case shows a gradient of z_+ which is due to the latitudinal gradient of PV.

In the central latitudes the upper limit to the vorticity is $\xi_{\max} \approx 5 \times 10^{-5}\, \text{s}^{-1}$. Using scaling relations and geostrophic balance (Holton 1992) this can be expressed as an equivalent pressure gradient,

$$\xi_{\max} = \frac{U}{L} = \frac{1}{L\rho f}\frac{(\Delta p_a)_{\max}}{L}$$

where U is a typical horizontal velocity, L is a length scale, ρ is the atmospheric density ($1\, \text{kg}\, \text{m}^{-3}$) and p_a is the atmospheric pressure. Using a synoptic length scale, $L = 10^6\, \text{m}$, and a mid-latitude Coriolis parameter, $f = 10^{-4}\, \text{s}^{-1}$, it is found that $(\Delta p_a)_{\max} = 50\, \text{mb}$. As an order of magnitude calculation this is in good agreement with the atmosphere, where the average sea-level pressure is $1013\, \text{mb}$, and there have been observations between 870 and $1075\, \text{mb}$ (Burt 2004).
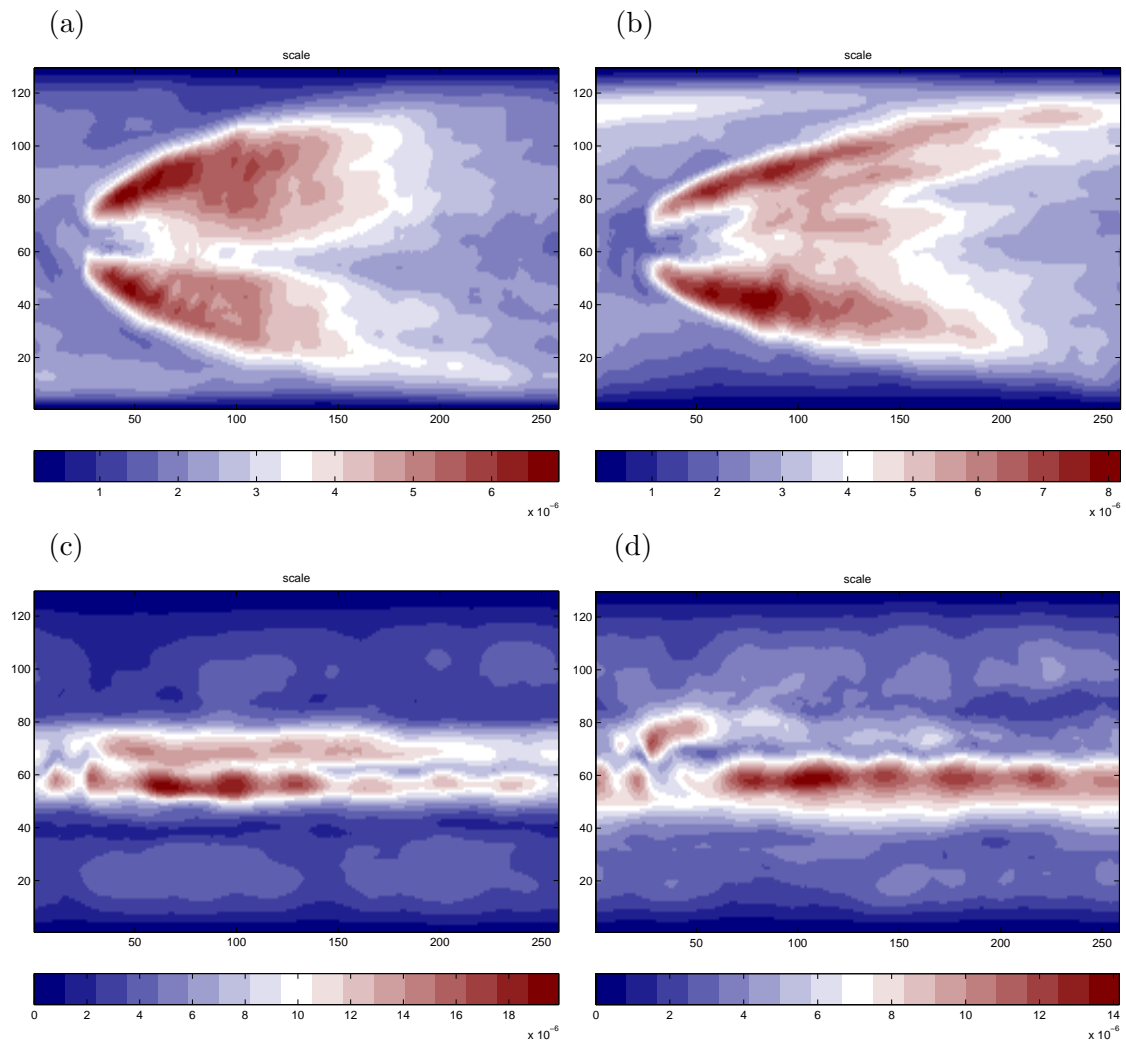
Figure 6.7: Maps of the estimated GEV distribution scale parameter, $\hat{\sigma}$ - (a) maxima for $\beta = 0$, (b) minima for $\beta = 0$, (c) maxima for $\beta > 0$, and (d) minima for $\beta > 0$.
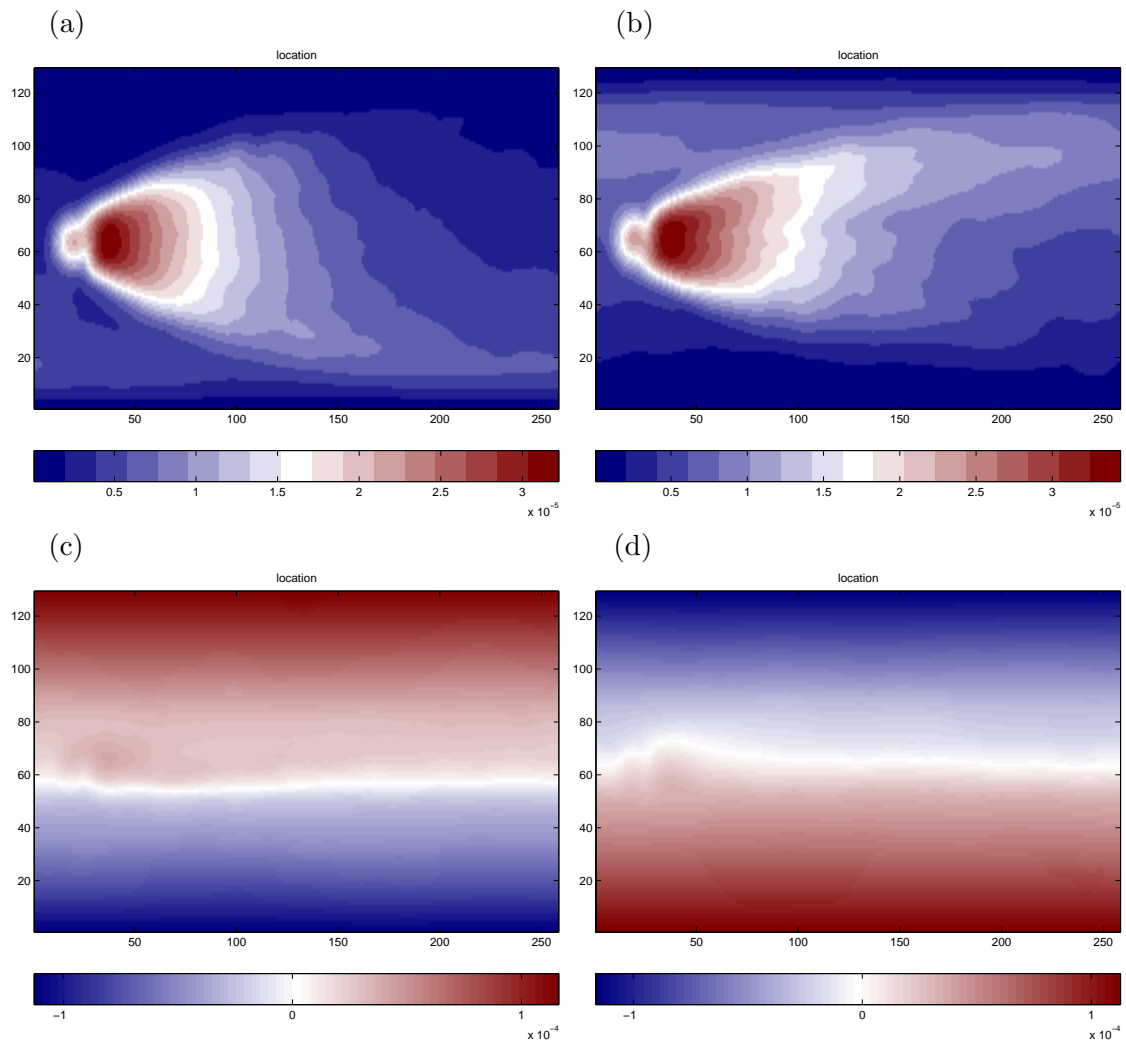
Figure 6.8: Maps of the estimated GEV distribution location parameter, $\hat{\mu}$ - (a) maxima for $\beta = 0$, (b) minima for $\beta = 0$, (c) maxima for $\beta > 0$, and (d) minima for $\beta > 0$.
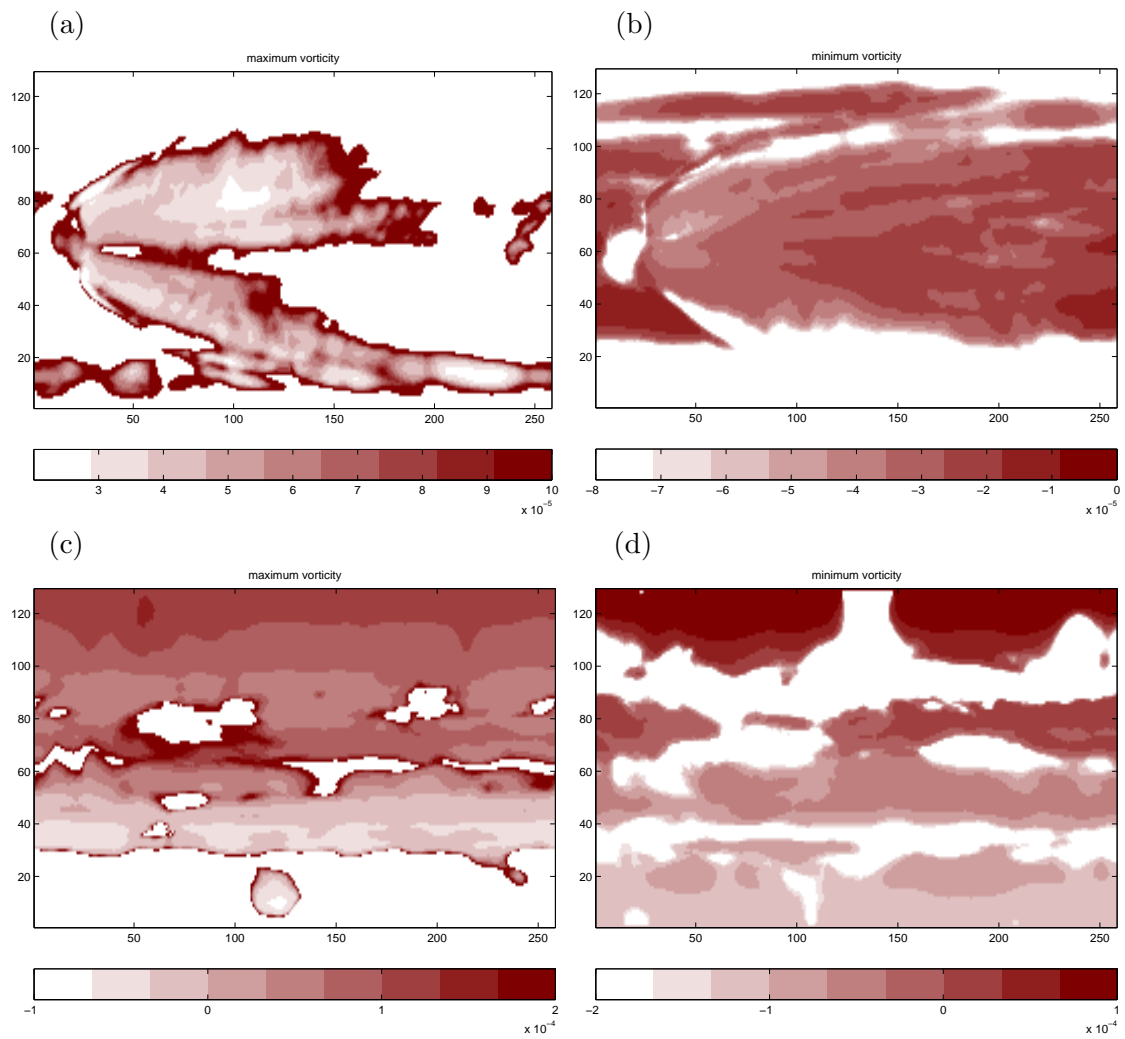
Figure 6.9: Maps of z_+ - (a) maximum for $\beta = 0$, (b) minimum for $\beta = 0$, (c) maximum for $\beta > 0$, and (d) Minimum for $\beta > 0$. Blank areas have infinite values.

6.4   Sensitivity to initial conditions

Fig. 6.10 shows the GEV distribution shape parameter ($\hat{\gamma}$) for four different starting random initial conditions - the first row is the model run already analysed, and shows the asymmetry between the maxima (left column) and minima (right column). The second row shows an asymmetry in the opposite direction with a generally more negative shape parameter in the maxima map than the minima map. The other two runs show a more symmetric shape parameter between the maxima and minima.

These results reflect the change in the mean vorticity shown in Fig. 5.10 with the runs with more symmetric maps of the mean with latitude also showing a more symmetric pattern in the shape parameters of the maxima and minima.

Resolving the reasons for this effect requires a more detailed analysis, including an ensemble of longer simulations.

6.5   Summary

It has been shown that the distribution of vorticity produced in these simulations is well fitted by a GEV distribution, with a block size of 10 days, for both the maxima and minima. It was also shown that the closed-form estimates of the GEV distribution parameters gave similar results to the maximum likelihood estimates, and were easier to calculate.

The estimated GEV distribution shape parameters are asymmetric with respect to the sign of vorticity in the two-dimensional turbulence simulation, but this is not highly significant, and is initial condition dependent. In the geostrophic turbulence case this asymmetry is not present, though there are strong variations of the shape parameter with latitude. In both simulations the scale and location parameters show similar features to those seen in the moment estimates.
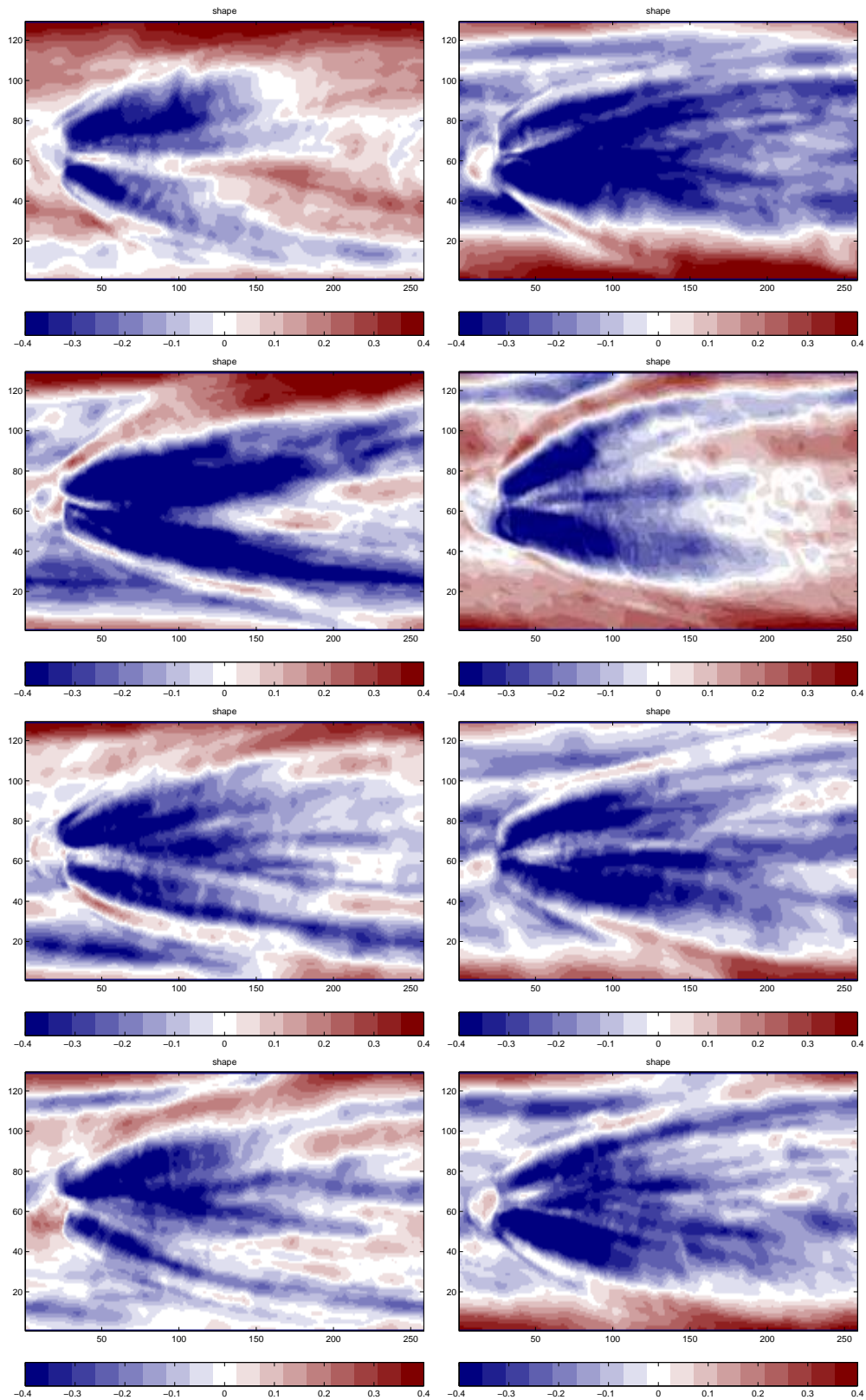
Figure 6.10: GEV distribution shape parameter for maxima (left column) and minima (right column) for four sets of initial conditions in two-dimensional turbulence.

Chapter 7

Conclusions and Future Directions

7.1 Conclusions

Charney et al. (1950) were the first to demonstrate that a simple numerical model of the barotropic vorticity equation can simulate certain features of the atmosphere. In this study, the addition to the model of a vorticity forcing at a single location is able to generate a surprisingly rich structure - this includes a storm track, 'jets' and different regimes of turbulence.

7.1.1 Features and moments of turbulence

The numerical model was able to successfully reproduce other authors findings (e.g. McWilliams 1990a) that two-dimensional turbulence generate coherent, isolated vortices which tend to merge. The measured kurtosis in this case is larger than for a Gaussian distribution, even with the forcing term and zonal flow aspects of this experiment which others have lacked.

The geostrophic model run generated a simple 'storm track' which propagated pressure systems eastwards in a similar way to the atmosphere. The 'jet' system bore a remarkable resemblance to the real atmosphere with alternating easterly and westerly streams. It was found, similarly to previous authors (McWilliams 1990a, McWilliams 1990b), that the scale of the vortices produced in geostrophic turbulence is slightly reduced compared to the two-dimensional case - this is due to the generation of Rossby waves. This also causes the kurtosis measured at a single point to be much reduced, as has been noted before. It was shown (Section 5.2) that the maps of standard moments estimated from the numerical simulations of the geostrophic turbulence qualitatively agreed with the observations of White (1980). In the central regions of the domain there were bands of low and high kurtosis which matched similar bands in the observations, and there was also a slight increase in skewness with latitude, again seen by White (1980) and Swanson (2001). There is also evidence for the bi-modality of the distribution of potential vorticity, which has been

observed in the atmosphere (Swanson 2001).

In common with previous authors (e.g. Nakamura and Wallace 1991), it was found that the standard higher order moments such as skewness and kurtosis tend to be dominated by a small number of extreme values (Appendix B.1). This was not so true for the quantile measures that were used, though these are harder to calculate.

7.1.2 Extremes of turbulence

It has been found that the distribution of vorticity in the model is well fitted by the theoretical GEV distribution away from the domain boundaries (Section 6.1.1), and so analysing the parameters of this distribution is a valid idea. It was shown that the closed form estimates and maximum likelihood estimates give very similar best fit parameters in most cases, though there instances when the maximum likelihood fit fails to converge. A more comprehensive optimisation routine might be able to correct this. The closed form estimates are far quicker and simpler to calculate and so it would suggest that this extra effort is not necessary.

Two-dimensional turbulence, $\beta = 0$

One of the more intriguing results of the $\beta = 0$ run presented was the asymmetry generated in the extreme shape parameter between the positive and negative vorticity tails. In the run presented, this asymmetry was similar to the atmosphere, in the sense that the low pressure systems could become more extreme than the high pressure systems - i.e. in the same sense as the atmosphere (Venn 1887).

But, it was also found that the evolution of vorticity was dependent on the initial conditions as one sign of vorticity tended to dominate in different cases. The asymmetric extremes conclusion is thus not as strong, and requires more analysis.

Geostrophic turbulence, $\beta > 0$

The maps of maxima and minima extreme shape parameters are very similar in the geostrophic run, and show no sign of the asymmetry observed in the two-dimensional case. The 'gradient wind balance' (Section 2.2) is thus not ruled out as an explanation for the observed asymmetry in the atmosphere.

There is evidence for a wave like structure of the GEV model distribution shape parameter with latitude which suggests that certain latitudes can experience more extreme variations than others. Using scaling relations the extremes of vorticity can be converted to extremes of atmospheric pressures. The model values are shown to give pressure changes comparable to the real extremes observed in the atmosphere.

7.2 Future directions

If there was more time, and more computing resources available then there are a number of further analyses and experiments that could be performed.

7.2.1 Simulation length

It is seen in the atmosphere that 'storm tracks' have cycles of periods of different strength and activity. This characteristic was also seen in both turbulence simulations - throughout the 1000 day model run there were different regimes. In this study these different regimes have been largely ignored in the statistical estimates. Scientifically it would be valuable to analyse each regime separately to see how the extremes vary in each case, and whether they are different. To do this a longer simulation would be needed to produce longer periods of each regime.

A longer simulation length would also help reduce the errors in the statistical estimates. Currently, the asymmetry of extremes seen in the two-dimensional case is not particularly significant. With more vorticity data this question could be resolved. Currently the simulation length encompasses around 4 winters, whereas the observations of White (1980) cover 11 winters and those of Swanson (2001) cover 40 winters. An increase of simulation length of a factor of ten may help to reduce the errors to about one-third of their current levels, and this may be small enough to rule out the null hypothesis that the extremes are symmetric.

The dependence upon initial conditions is another question which an increased length of simulation would help resolve. Does the model flip between states during a simulation? Or is it locked in one state due to the initial conditions? This is the question of 'intransitivity' (Lorenz 1970).

7.2.2 Passive tracer

The numerical model created for this study also included a passive tracer - a variable which was advected with the flow but had no impact on the flow itself - in the atmosphere this could be a particular gas or pollutant. There was not enough time to analyse the data from this part of the model in this study. The scientific motivation for including a tracer was to test if the extremes of a tracer matched those of vorticity. Fig. 7.1 shows a snapshot of the distribution of the passive tracer in the geostrophic turbulence case, after 500 days of the model - it shows clear signs of 'mixing', rather like cream in coffee!

Passive tracer experiments have been performed numerically before, e.g. Bartello and Holloway (1991), and has a particular application to the spread of pollutants. It has been found in observations (White 1980) that the distribution of the streamfunction remained approximately Gaussian even when the distribution of vorticity was strongly flattened. It
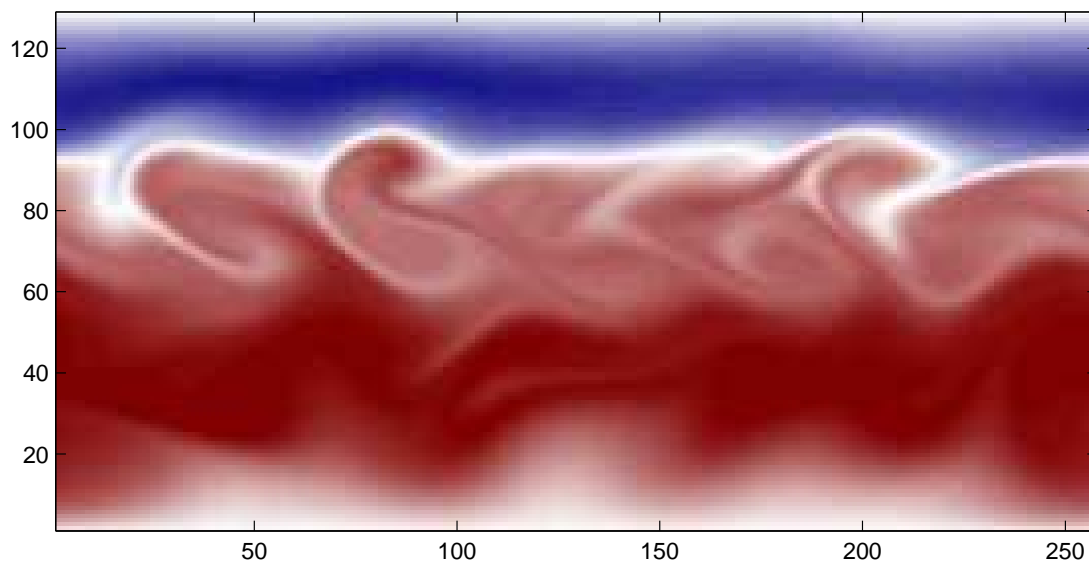
Figure 7.1: Snapshot of the distribution of passive tracer in geostrophic turbulence.

would be interesting to see if a passive tracer in the numerical model acted in the same way.

7.2.3 Increase of horizontal resolution

The major weather centres are continually aiming to increase the resolution of their models in an effort to more accurately predict the weather. The UK Met Office had a particular interest after the Boscastle floods of 2004 which were not well predicted by the mesoscale model in operation. A high resolution model run after the event was able to predict the extreme rainfall to a much higher accuracy (e.g. Roberts 2005).

This numerical model could be used for further experiments using different resolutions to see how the extremes vary - will they pick up the more extreme events that are not seen at poorer resolutions? This would require starting from identical initial conditions, sampled onto the different grids.

7.2.4 Latitudinal variation

The study performed here has had a mid-latitude (i.e. UK) bias with the selection of the effective latitude for the geostrophic simulation. This was mainly due to the location of the storm track on Earth. A different value of β, and a change of resolution, would move the model to a different latitude, and it would be interesting to see how the model reacts to this. This would also examine in more detail how the extremes vary with latitude.

Appendix A

Numerical Model Design

A.1 The barotropic equation algorithm

This algorithm is a much modified version of that used for the 'Numerical Modelling' module, MTMW14.

A.1.1 Design

Once the numerical scheme was decided, it was then necessary to code up the model. From the initial conditions of vorticity and streamfunction the following sequence is implemented:

- Step 1: Use the numerical scheme (Eqn. 3.7) to calculate the new vorticity field.
- Step 2: Apply boundary conditions to the new vorticity field.
- Step 3: Invert the Poisson equation (Eqn. 3.4) to obtain the streamfunction.
- Step 4: Use the streamfunction to calculate the new velocities (Eqn. 3.3).
- Step 5: Apply boundary conditions on the new velocities (Eqns. 3.8, 3.9)
- Step 6: Return to Step 1.

A.1.2 Initial testing of the model

A number of checks were performed to ensure that the model was working as expected. Primarily this involved 'turning off' various terms in the equation to ensure that the model was behaving as it should, e.g. having just advection, or just diffusion. Next it was confirmed by observation that the wind directions always remained parallel to the streamfunction contours, and that they circulated in the correct direction, i.e. in an anticyclonic direction around negative vorticity regions and vice versa. It was also noted that if we moved the model into the Southern Hemisphere (i.e. by making the value of f_0 negative), then the winds and advection were reversed, as expected.
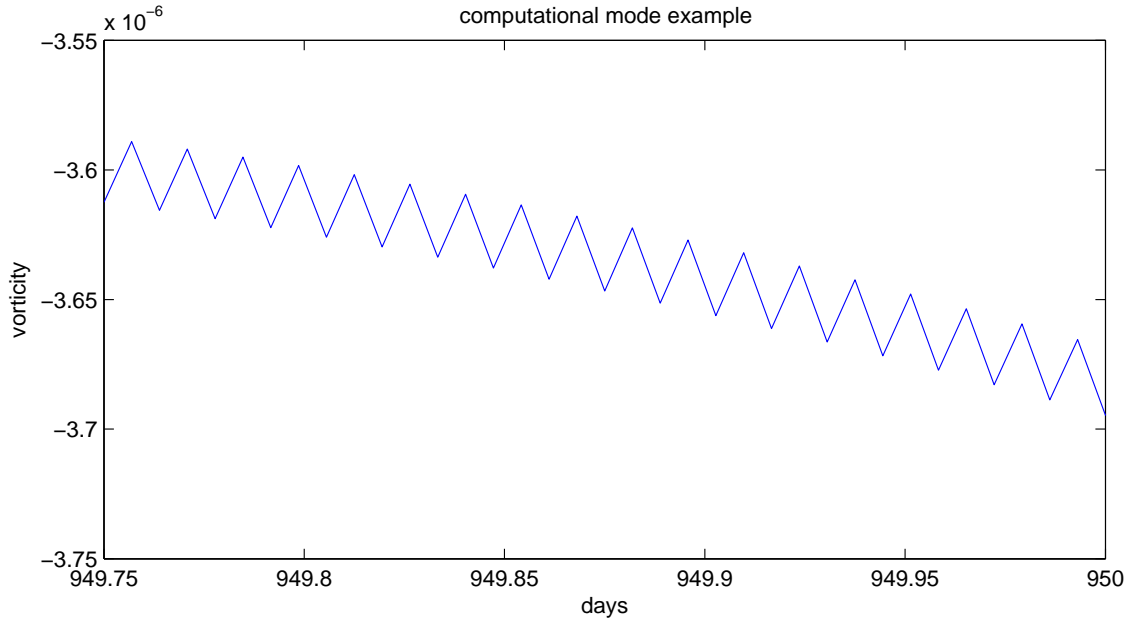
Figure A.1: The computational mode of the numerical scheme. The blue line is a unfiltered version of the vorticity at a single point over the time range indicated.

A.1.3   Computational mode of the numerical scheme

When using a centred temporal scheme it is inevitable that there is an extra solution to the finite difference equations. This 'computational mode' is an artifact of the numerical scheme, and is normally oscillatory. The blue line in Fig. A.1 shows the vorticity at a particular point for a small time range, and shows the computational mode which appears superimposed on the physical mode. It can be seen that the mode is small ($\sim 0.2\%$) and this is partly due to the diffusion term in the equations which helps to damp out the oscillations. There are known filtering techniques to help reduce the computational mode further (e.g. Asselin 1972), but these are time consuming in the code. Due to the size of the effect it is not considered necessary to implement the filter in our numerical scheme.

A.2   Tuning of model parameters

A.2.1   Length of timestep

The choice of timestep is crucial to ensuring that the numerical scheme produces a stable solution. Fig. A.2 shows the stencil of the numerical scheme (Eqn. 3.7) in one space dimension. CFL conditions (Courant et al. 1928) dictate that the highest velocity waves (i.e. largest values of u) must remain inside the stencil to ensure stability. Thus,

$$\Delta t \leq \frac{\Delta x}{2u_{\max}}$$

for stability. Using the fixed value for $\Delta x \approx 100.0\,\text{km}$ and $u_{\max} \approx 30\,\text{m s}^{-1}$, then it is found that $\Delta t \lesssim 30\,\text{mins}$. The timestep used was $\Delta t = 10\,\text{mins}$ to be comfortably inside this limit and to increase accuracy. Smaller values of timestep would make the model prohibitively long to run. If a smaller timestep was required by CFL conditions then a Lagrangian or semi-Lagrangian scheme would have to be used, but these are far more complicated.
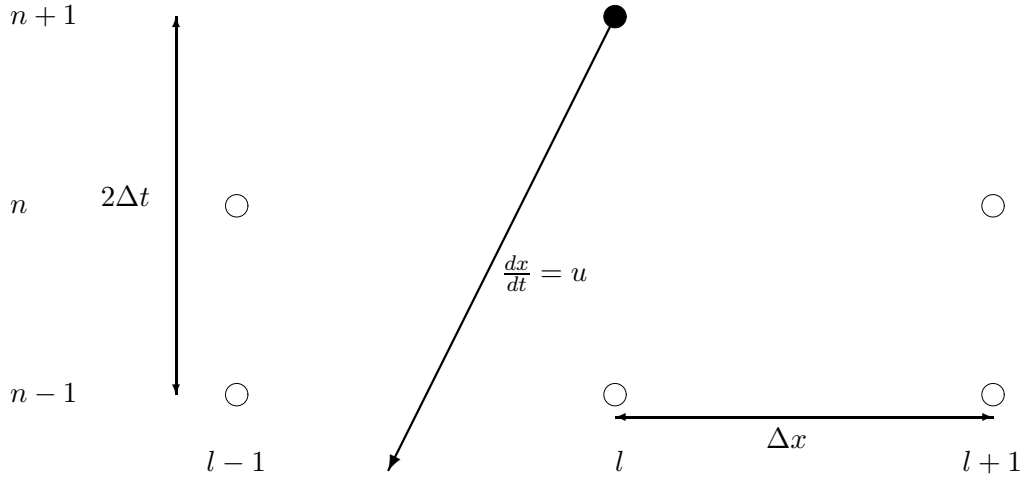

Figure A.2: The stencil of the numerical scheme in one dimension, with known quantities shown as unfilled circles, and the unknown quantity shown as a filled circle. The time levels are denoted as n and the space levels with l.

A.2.2 Diffusion and forcing

To ensure that the model didn't die out due to the diffusion it was necessary to balance the forcing and diffusion parameters. The diffusion parameter had to be large enough to ensure that 'spectral blocking' did not cause the model to 'blow up'. The forcing 'hill' parameters had to be realistic values for a mountain range. From these constraints, and by some experimentation the values chosen for the parameters were,

$$
\begin{aligned}
\kappa &= 5 \times 10^5\,\text{m}^2\,\text{s}^{-1} \quad (\beta = 0) \\
\kappa &= 1 \times 10^5\,\text{m}^2\,\text{s}^{-1} \quad (\beta > 0) \\
h_0 &= 2500\,\text{m}, \\
r &= 800\,\text{km}.
\end{aligned}
$$

The diffusion parameter for the $\beta > 0$ case is lower than that for the $\beta = 0$ case as there is some natural smoothing of the vorticity field due to the Rossby waves generated by the β-effect.

Appendix B

Numerical Model Testing

B.1 Simulation length

Choosing the length of the model run was achieved by needing enough data to ensure the statistics are robust, but with the limits of time to perform the runs, and disk space to consider. The time of 1000 days was chosen, with a 'spin-up' time of 300 days, leaving 700 days for the statistics to be calculated over. It has been checked that the measured statistics do not change very significantly for slightly different values of the 'spin-up' time.

The time of 300 days for the 'spin-up' was chosen, partly by examining the time lapse movie (not shown) of the run, and partly by examining the cumulative moments like those shown in Fig. B.1. The panels show the standard moments calculated cumulatively, starting at the end of the run, e.g. the point plotted at 500 days is the cumulative moment for the data from 500 – 1000 days etc. The lower moments show a fair amount of variation, with the mean being affected strongly by the different activity regimes in the run. The values at large time points are noisy as there are few data points involved.

One of the most striking features of the plots for the higher moments are the large jumps in skewness and kurtosis, e.g. at about 475 days. This demonstrates how a few extreme values can affect the moment values far more significantly than might be expected. As previously discussed, this was also noted by Nakamura and Wallace (1991) in their observations of geopotential height, where the extreme values dominated the values of skewness they observed. Using the quantile moments (not shown) the jumps are far less significant, as expected, due to the measures being less dependent on individual events and they can be considered more robust to extreme values (or 'outliers').
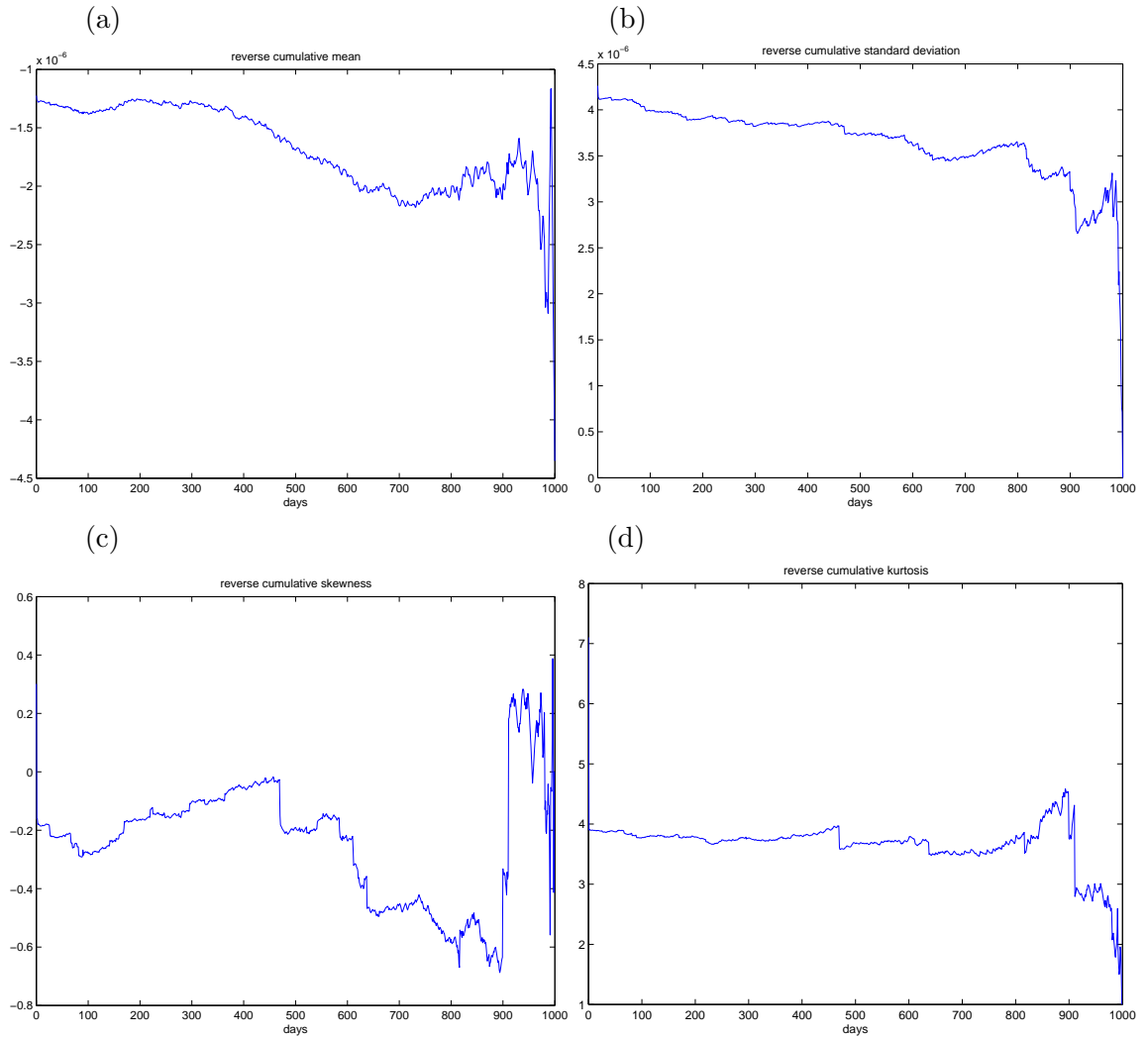
Figure B.1: Reverse cumulative calculations for two-dimensional turbulence of (a) the mean, (b) the standard deviation, (c) the skewness, and (d) the kurtosis. These are measured starting at the end of the run, for a single point ($x = 200, y = 64$).

B.2 Sampling frequency

It was noted (not shown) that using the data at every model day, instead of every timestep, created a strong aliasing signature in the standard and quantile moment plots. This was due to the 3-day periodic forcing and shows that using the data once a day is clearly not adequate to sample the data. It is therefore important to use more frequent data. This is not possible for the quantile moments (see Section 4.2) due to restrictions on disk space as the data at every timestep needs to be stored for each grid point.

B.3 Estimating an optimal block size

When using a GEV distribution to consider extremes, Section 4.3.2 describes how it is necessary to estimate an optimal block size to take the maxima and minima over. It was also shown that the shape parameter should remain constant with block size, assuming the block size is large enough to be representative. Fig. B.2 shows the estimated shape parameter as a function of block size for both maxima and minima, and for both versions of the model. The red line is the closed-form estimate of the shape parameter, with 95% confidence intervals shown dashed. The blue line is the maximum likelihood estimate of the shape parameter.

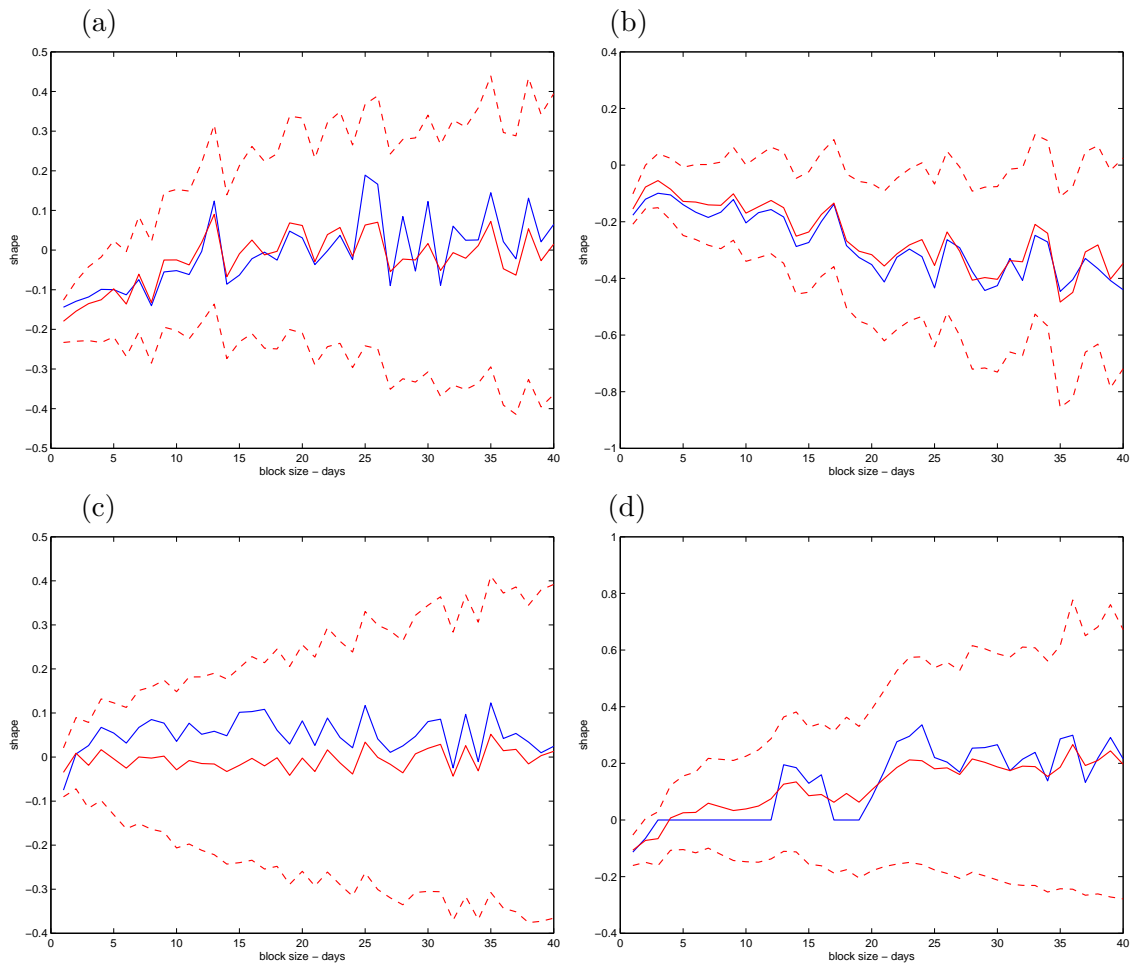In all cases it is seen that after 10 days, the shape parameter remains constant with

Figure B.2: Shape parameter for varying block sizes for a single representative point - (a) maxima for $\beta = 0$, (b) minima for $\beta = 0$, (c) maxima for $\beta > 0$, and (d) minima for $\beta > 0$. The red line is the closed-form estimate of the shape parameter, with 95% confidence intervals shown dashed. The blue line is the maximum likelihood estimate of the shape parameter.

increasing block size, within the confidence intervals shown. For block sizes less than 10 days the shape parameter is often not constant. The confidence intervals become larger with increasing block size as there are less points to fir the GEV distribution to. A block size of 10 days is hence chosen as a suitable size for this experiment.

The figures also show that, in the two-dimensional turbulence experiment, both the maximum likelihood and closed-form estimates agree, which gives us confidence in their use. In the geostrophic experiment the agreement is not as close, and it was noted that the maximum likelihood fit had more trouble converging in this case. It is decided to use the closed-form estimates predominantly, as they are easier to calculate, and they also allow approximate confidence intervals to be estimated.

Bibliography

Asselin, R., 1972. Frequency filter for time integrations. Mon. Weather Rev., **100**, 487–490.

Bartello, P., Holloway, G., 1991. Passive scalar transport in β-plane turbulence. J. Fluid Mech., **223**, 521–536.

Batchelor, G. K., 1967. *Introduction to Fluid Dynamics*. Cambridge University Press.

Bjerknes, V., 1904. Das problem von der wettervonhersage betrachtet vom standpunkt der mechanik und der physik. Meteor. Z., **21**, 1–7.

Burt, C. C., 2004. *Extreme Weather, A Guide and Record Book*. W. W. Norton and Co.

Charney, J. G., 1971. Geostrophic turbulence. J. Atmos. Sci., **28**, 1087–1095.

Charney, J. G., Fjörtoft, R., von Neumann, J., 1950. Numerical Integration of the Barotropic Vorticity Equation. Tellus, **2**, 237–254.

Coles, S., 2001. *An Introduction to Statistical Modeling of Extreme Values*. Springer.

Courant, R., Friedrichs, K., Lewy, H., 1928. Über die partillen Differentialgleichungen der mathematischen Physik. Math. Ann., **100**, 32–74.

Easterling, D. R., Meehl, G. A., Parmesan, C., Changnon, S. A., Karl, T. R., Mearns, L. O., 2000. Climate extremes: Observations, modeling, and impacts. Science, **289**, 2068–2074.

Fjörtoft, R., 1953. On the changes in the spectral distribution of kinetic energy for two-dimensional non-divergent flow. Tellus, **5**, 225–230.

Holton, J. R., 1992. *An Introduction to Dynamic Meteorology*. Academic Press.

Hosking, J. R. M., Wallis, J. R., Wood, E. F., 1985. Estimation of the generalized extreme-value distribution by the method of probability-weighted moments. Techometrics, **27**, 251–261.

IPCC, 2001. *Third Assessment Report*. Cambridge University Press.

Jenkinson, A. F., 1955. The frequency distribution of the annual maximum (or minimum) values of meteorological elements. Q.J.R. Met. S., **81**, 158–171.

Kraichnan, R. H., Montgomery, D., 1980. Two-dimensional turbulence. Rep. Prog. Phys., **43**, 547–619.

Lean, H. W., Ballard, S. P., Clark, P. A., Dixon, M. A. G., Li, Z., Roberts, N. M., 2005. The summer 2003 reruns with the high resolution trial model. Met. Office Forecasting Research Technical Reports, No. 457.

Lilly, D. K., 1969. Numerical simulation of two-dimensional turbulence. Phys. Fluids, **Suppl. II**, 240–249.

Lorenz, E. N., 1970. Climate change as a mathematical problem. J. App. Met., **9**, 325–29.

Maltrud, M. E., Vallis, G. K., 1991. Energy spectra and coherent structures in forced two-dimensional and beta-plane turbulence. J. Fluid Mech., **228**, 321–342.

McWilliams, J., 1983. On the relevance of two-dimensional turbulence to geophysical fluid motions. Journal de Mécanique Théorique et Appliquée, **Sp. Issue**, 83–97.

McWilliams, J., 1984. The emergence of isolated coherent vortices in turbulent flow. J. Fluid Mech., **146**, 21–43.

McWilliams, J., 1990a. The vortices of two-dimensional turbulence. J. Fluid Mech., **219**, 361–386.

McWilliams, J., 1990b. The vortices of geostrophic turbulence. J. Fluid Mech., **219**, 387–404.

Moors, J. J. A., 1988. A quantile alternative for kurtosis. The Statistician, **37**, 25–32.

Nadarajah, S., 2005. Extremes of daily rainfall in West Central Florida. Clim. Change, **69**, 325–342.

Nakamura, H., Wallace, J. M., 1991. Skewness of low-frequency fluctuations in the tropospheric circulation during the Northern Hemisphere winter. J. Atmos. Sci., **48**, 1441–1448.

Palutikof, J. P., Brabson, B. B., Lister, D. H., Adcock, S. T., 1999. A review of methods to calculate extreme wind speeds. Met. Appl., **6**, 119–132.

Proudman, J., 1916. On the motion of solids in liquids possessing vorticity. Proc. R. Soc., **92**, 408–424.

Rhines, P. B., 1975. Waves and turbulence on a beta plane. J. Fluid Mech., **69**, 417–443.

Rhines, P. B., 1979. Geostrophic turbulence. Ann. Rev. Fluid Mech., **11**, 401–441.

Richardson, L. F., 1922. *Weather Prediction by Numerical Process.* Cambridge University Press.

Roberts, N., 2005. An investigation of the ability of a storm scale configuration of the Met. Office NWP model to predict flood-producing rainfall. Met. Office Forecasting Research Technical Reports, No. 455.

Rossby, C.-G., 1939. Relation between variations in the intensity of the zonal circulation of the atmosphere and the displacements of the semi-permanent centers of action. J. Marine Res., **2**, 38–55.

Schär, C., Vidale, P. L., Lüthi, D., Frei, C., Häberli, C., Liniger, M. A., Appenzeller, C., 2004. The role of increasing temperature variability in European summer heatwaves. Nature, **427**, 332–336.

Smith, P., 1995. A recursive formulation of the old problem of obtaining moments from cumulants and vice versa. The Am. Stat., **49**, 217–218.

Stott, P. A., Stone, D. A., Allen, M. R., 2004. Human contribution to the European heatwave of 2003. Nature, **432**, 610–614.

Swanson, K. L., 2001. Upper-tropospheric potential vorticity fluctuations and the dynamical relevance of the time mean. J. Atmos. Sci., **58**, 1815–1826.

Tung, K. K., Orlando, W. W., 2003. On the differences between 2D and QG turbulence. Discrete and Continuous Dynamical Systems - Series B, **3**, 145–162.

Venn, J., 1887. The law of error. Nature, **36**, 411–412.

White, G. H., 1980. Skewness, kurtosis and extremes of Northern Hemisphere geopotential height. Mon. Weather Rev., **108**, 1446–1455.

Williams, G. P., 1978. Planetary circulations. I - Barotropic representation of Jovian and terrestrial turbulence. J. Atmos. Sci., **35**, 1399–1426.